

Theoretical foundations of triboelectric nanogenerators (TENGs)

SHAO JiaJia^{1,2†}, JIANG Tao^{1,2†} & WANG ZhongLin^{1,2,3*}¹ *Beijing Institute of Nanoenergy and Nanosystems, Chinese Academy of Sciences, Beijing 100083, China;*² *School of Nanoscience and Technology, University of Chinese Academy of Sciences, Beijing 100049, China;*³ *School of Materials Science and Engineering, Georgia Institute of Technology, Atlanta GA 30332-0245, USA*

Received March 14, 2020; accepted April 15, 2020; published online May 28, 2020

Triboelectric nanogenerator (TENG) is an emerging powerful technology for converting ambient mechanical energy into electrical energy through the effect of triboelectricity. Starting from the expanded Maxwell's equations, the theoretical framework of TENGs has been gradually established. Here, a review is given about its recent progress in constructing of this general theory. The fundamental mechanism of TENGs is constructed by the driving force—Maxwell's displacement current, which is essentially different from that of electromagnetic generators. Theoretical calculations of the displacement current from a three-dimensional mathematical model are presented, as well as the theoretical studies on the TENGs according to the capacitor models. Furthermore, the figure-of-merits and standards for quantifying the TENG's output characteristics are discussed, which will provide important guidelines for optimizing the structure and performance of TENGs toward practical applications. Finally, perspectives and challenges are proposed about the basic theory of TENGs and its future technology development.

triboelectric nanogenerator, theoretical foundations, displacement current, three-dimensional model, capacitor model, figure-of-merits

Citation: Shao J J, Jiang T, Wang Z L. Theoretical foundations of triboelectric nanogenerators (TENGs). *Sci China Tech Sci*, 2020, 7, <https://doi.org/10.1007/s11431-020-1604-9>

1 Introduction

Energy is one of the most important resources marking the quality of human life. With the continuous consumption of traditional fossil fuels, humans will face serious energy crises [1]. Besides the macro energy supply such as public transportation and factories, all kinds of portable electronics and recently emerging internet of things and sensor networks all need to be powered. Although these micro devices have low demands for energy, their quantity is huge, and they are widely distributed in every corner of the world. At present, powering the micro devices mainly relies on rechargeable batteries. However, with the increase in the number and density of mobile electronic devices, the demands for the

number of batteries will increase rapidly, bringing many severe problems such as battery recycling and waste battery pollution. Therefore, it is of practical significance to develop micro/nano scale energy technology to harvest energy from surrounding environment [2], and then realize the self-powering of electronic devices.

The idea of self-powering was first proposed by Wang in 2006 as a result of invention of piezoelectric nanogenerator (PENG) [3]. The first PENG converted the tiny mechanical deformation energy into electric energy when a mechanical force was applied to a single zinc oxide nanowire. This milestone study has inspired the field of nanoenergy [4], which is about the harvest, storage and effective utilization of energy in our living environment using nanomaterials, nanodevices and nanosystems. Another nanogenerator, triboelectric nanogenerator (TENG) was first invented by Wang in 2012 [5], based on the coupling effect of triboelec-

†These authors contributed equally to this work.

*Corresponding author (email: zlwang@gatech.edu)

trification and electrostatic induction. As a promising mechanical energy harvesting technology, the TENG has obvious advantages of high power density, high efficiency, low weight and low fabrication cost relative to traditional electromagnetic generator (EMG) [6–9]. The output power of EMG is proportional to the square of frequency, while that of TENG is proportional to frequency [10]. So, at low frequency the output power of TENG is much higher, and the TENG is the better choice. So far, a large number of TENG devices have been designed and fabricated to harvest environmental mechanical energy from various sources, such as human motion [11], mechanical vibration [12], wind [13,14] and ocean waves [15–21], and so on. The researches on the TENGs as power sources and self-powered sensors have attracted worldwide interests due to their important applications for internet of things, sensor network, artificial intelligence, medical sciences, implantable devices, as well as environmental protection system [22]. Importantly, the TENG technology provides a route toward the energy for the new era—the era of internet of things and sensor networks [23,24].

Recently, theoretical models have been built for different working modes of TENGs, including the contact-separation [25], lateral-sliding [26], single-electrode [27], and free-standing modes [28], based on which finite element simulations and theoretical calculations have been systematically carried out. Firstly, the theoretical researches mainly rely on the traditional parallel-plate capacitor (CA) models. Although the CA model can provide useful guidelines for the optimization of structure and performance of the TENG devices as well as their practical applications, this model is still limited because of its built just from the circuit theory and only focusing on one single relative motion process. Until 2017, the theoretical origin of nanogenerators has been demonstrated to be the Maxwell's displacement current by Wang [23, 29], which is essentially different from that of EMG adopting the mechanism of resistive free electron conduction driven by Lorentz force. An additional term \mathbf{P}_s , denoting the polarization created by the electrostatic surface charges, has been introduced into the electric displacement vector \mathbf{D} , and a second term $\partial\mathbf{P}_s/\partial t$ has been added into the expression of displacement current, which is the application of Maxwell's equations in energy and sensors [30]. Given this, the expanded Maxwell's equations due to the new additional term \mathbf{P}_s , also called as Wang term, can serve as the first principle theory for quantifying the output and electromagnetic behavior of nanogenerators. However, the quantitative details and insight on how the variation of the three-dimensional (3D) spatially-distributed electric displacement affects the generation of the displacement current, for different TENG mode geometries, have not yet been addressed. So, from the point of classical electrodynamics, a simple time-dependent 3D mathematical model is proposed. Based

on the 3D model, not only the generation and variation of the Maxwell's displacement current, but also the basic characteristics of the alternating current (AC) of TENGs have been numerically calculated, while some special geometric cases are derived analytically [31–34]. Henceforth, the fundamental theoretical framework of TENGs for a general case is finally built.

Here, recent progress in constructing the theoretical foundations of triboelectric nanogenerators is reviewed. The review focuses on the nanogenerator theories established from expanded Maxwell's equations, theoretical calculations of the Maxwell's displacement current, standards and figure-of-merits of TENGs, and future perspectives in TENG theory expansion and technology development. In the first segment of the review, the fundamental mechanism of nanogenerators is demonstrated through expanding the Maxwell's equations. Subsequently, we devote to elaborating on theoretical calculations of the Maxwell's displacement current and characteristics of the alternating current of TENGs from the 3D mathematical model, followed by the progress of TENG's basic output performances from the CA model. In the next section, by combining the theoretical and experimental methods, the figure-of-merits of TENGs are defined, and standards for quantifying the TENG performance are established. Finally, some perspectives and challenges for the theory expansion of TENGs and its practical implications are discussed.

2 Theories of nanogenerators from Maxwell's equations

Recently, the theories for nanogenerators have been formally established by Wang [23,29,30] starting from the Maxwell's equations, which have the following basic forms:

$$\nabla \cdot \mathbf{D} = \rho, \quad (1a)$$

$$\nabla \cdot \mathbf{B} = 0, \quad (1b)$$

$$\nabla \times \mathbf{E} = -\frac{\partial \mathbf{B}}{\partial t}, \quad (1c)$$

$$\nabla \times \mathbf{H} = \mathbf{J} + \frac{\partial \mathbf{D}}{\partial t}, \quad (1d)$$

where the displacement current, $\partial\mathbf{D}/\partial t$, was first introduced by Maxwell in 1861 to satisfy the continuity equation for electric charges [35]. The electric displacement \mathbf{D} is given by $\mathbf{D} = \varepsilon_0\mathbf{E} + \mathbf{P}$, and for an isotropic dielectric medium, $\mathbf{P} = (\varepsilon - \varepsilon_0)\mathbf{E}$, thus $\mathbf{D} = \varepsilon\mathbf{E}$. The displacement current density is presented as

$$\mathbf{J}_D = \frac{\partial \mathbf{D}}{\partial t} = \varepsilon \frac{\partial \mathbf{E}}{\partial t}. \quad (2a)$$

By adding the term \mathbf{P}_s in \mathbf{D} , i.e., $\mathbf{D} = \varepsilon_0\mathbf{E} + \mathbf{P} + \mathbf{P}_s$, the displacement current density is obtained by

$$\mathbf{J}_D = \frac{\partial \mathbf{D}}{\partial t} = \varepsilon \frac{\partial \mathbf{E}}{\partial t} + \frac{\partial \mathbf{P}_s}{\partial t}. \quad (2b)$$

Note that, the new additional term \mathbf{P}_s , also called as Wang term, is the polarization created by the electrostatic surface charges owing to mechanical triggering, which is different from that of the electric field induced medium polarization \mathbf{P} [30]. Then the Maxwell's equations have been rewritten as follows [30]:

$$\varepsilon \nabla \cdot \mathbf{E} = \rho - \nabla \cdot \mathbf{P}_s, \quad (3a)$$

$$\nabla \cdot \mathbf{B} = 0, \quad (3b)$$

$$\nabla \times \mathbf{E} = -\frac{\partial \mathbf{B}}{\partial t}, \quad (3c)$$

$$\nabla \times \mathbf{H} = \mathbf{J} + \varepsilon \frac{\partial \mathbf{E}}{\partial t} + \frac{\partial \mathbf{P}_s}{\partial t}. \quad (3d)$$

These equations are the cornerstones for deriving the output characteristics of nanogenerators, from which the output current, voltage, and related electromagnetic radiation of nanogenerators have all been derived.

The displacement current in the nanogenerators can be calculated by a surface integral of \mathbf{J}_D in eq. (2b):

$$\begin{aligned} I_D &= \int \mathbf{J}_D \cdot d\mathbf{s} = \int \frac{\partial \mathbf{D}}{\partial t} \cdot d\mathbf{s} = \frac{\partial}{\partial t} \int (\nabla \cdot \mathbf{D}) dr \\ &= \frac{\partial}{\partial t} \int \rho dr = \frac{\partial Q}{\partial t}, \end{aligned} \quad (4)$$

where Q is the total free charge amount on the electrode. From eq. (4), it can be known that the displacement current dominates the internal circuit in nanogenerators, while the capacitive conduction current dominates the external circuit. The internal circuit and external circuit can meet at the two electrodes, forming a complete loop. In particular, the displacement current is equal to the conduction current in the external circuit, which is important for understanding the nature of nanogenerators. The schematic illustration for the fundamental physics mechanisms of the nanogenerators is shown in Figure 1, which also presents a comparison of the mechanism between the EMG and nanogenerators. The nanogenerators, based on the piezoelectric/pyroelectric and triboelectric/electrostatic/electret effects, adopt the mechanism of Maxwell's displacement current. Therefore, nanogenerators can represent a field that uses displacement current as the driving force for effectively converting mechanical energy into electric power/signal. In contrast, the EMG is dominated by the conduction current. Although their mechanisms are different, they are unified by the Maxwell's equations.

In the expanded Maxwell's equations, the surface polarization density \mathbf{P}_s can be expressed by the following equation, when defining the charge density function $\sigma_s(\mathbf{r}, t)$ on the media surface by a shape function of $f(\mathbf{r}, t) = 0$ as illustrated in Figure 2(a).

$$\nabla \cdot \partial \mathbf{P}_s = -\sigma_s(\mathbf{r}, t) \delta(f(\mathbf{r}, t)), \quad (5a)$$

where the delta function $\delta(f(\mathbf{r}, t))$ is introduced to confine the shape of the media $f(\mathbf{r}, t) = 0$. So that the polarization charges produced by nonelectric field are confined on the media surface, which can be defined by

$$\delta(f(\mathbf{r}, t)) = \begin{cases} \infty & \text{if } f(\mathbf{r}, t) = 0, \\ 0 & \text{otherwise,} \end{cases} \quad (5b)$$

$$\int_{-\infty}^{\infty} \delta(f(\mathbf{r}, t)) dn = 1, \quad (5c)$$

where \mathbf{n} is the normal direction of the local surface, and dn is an infinitesimal along the surface normal direction of the media. Through solving the scalar electric potential $\phi_s(\mathbf{r}, t)$ from the surface charges

$$\phi_s(\mathbf{r}, t) = \frac{1}{4\pi} \int \frac{\sigma_s(\mathbf{r}', t')}{|\mathbf{r} - \mathbf{r}'|} ds', \quad (6)$$

the \mathbf{P}_s can be obtained by

$$\begin{aligned} \mathbf{P}_s &= -\nabla \phi_s(\mathbf{r}, t) \\ &= \frac{1}{4\pi} \int \sigma_s(\mathbf{r}', t') \frac{\mathbf{r} - \mathbf{r}'}{|\mathbf{r} - \mathbf{r}'|^3} ds' \\ &\quad + \frac{1}{4\pi c} \int \frac{\partial \sigma_s(\mathbf{r}', t')}{\partial t'} \frac{\mathbf{r} - \mathbf{r}'}{|\mathbf{r} - \mathbf{r}'|^2} ds', \end{aligned} \quad (7)$$

This is the general expression of the \mathbf{P}_s in eq. (3a) and (3d).

The current transport behavior of any configuration of nanogenerators connected with a load resistor (Figure 2(a)) can be derived by the following general equation:

$$\phi_{AB} = \int_A^B \mathbf{E} \cdot d\mathbf{L} = \frac{\partial Q}{\partial t} R, \quad (8)$$

where ϕ_{AB} is the potential drop from A electrode to B electrode, and integral $d\mathbf{L}$ is over a path from point A to point B. Note that this is an extremely key and basic equation, mainly because it can link the internal circuit and external circuit in any configuration of nanogenerator system. The current transport equation for a piezoelectric nanogenerator (Figure 2(b)) is

$$RA \frac{d\sigma}{dt} + z \frac{\sigma - \sigma_p}{\varepsilon} = 0, \quad (9)$$

where A is the electrode area, z is the piezoelectric film thickness, and σ_p is the polarization charge density. The current transport equation for the TENG in a contact-separation mode (Figure 2(c)) is

$$\begin{aligned} AR \frac{\partial \sigma(z, t)}{\partial t} &= -\sigma(z, t)(d_1/\varepsilon_1 + d_2/\varepsilon_2) \\ &\quad - H(t)(\sigma(z, t) - \sigma_T)/\varepsilon_0, \end{aligned} \quad (10)$$

where $H(t)$ is a function dependent on the contacting rate between the two dielectrics; d_1 and d_2 represent the thickness of the two different dielectric materials with the relative dielectric constants ε_1 and ε_2 , respectively; ε_0 is the permittivity of vacuum. Based on the transport equation, the displacement current, electric potential, output current and output power can be calculated for four basic TENG modes.

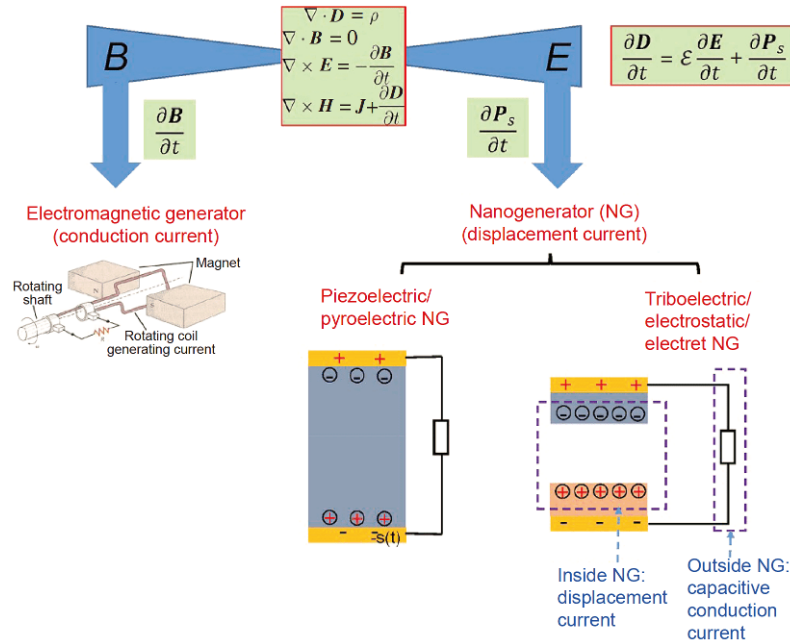


Figure 1 (Color online) Schematic illustration for the comparison of the fundamental physics mechanism between the electromagnetic generator and nanogenerator. The electromagnetic generator is dominated by the conduction current, while the nanogenerator is originated from the Maxwell's displacement current. Inside the nanogenerator, based on piezoelectric/pyroelectric and triboelectric/electrostatic/electret effects, the circuit is dominated by the displacement current, but the observed current outside the nanogenerator is the capacitive conduction current. Reproduced with permission [30]. Copyright 2020, Elsevier.

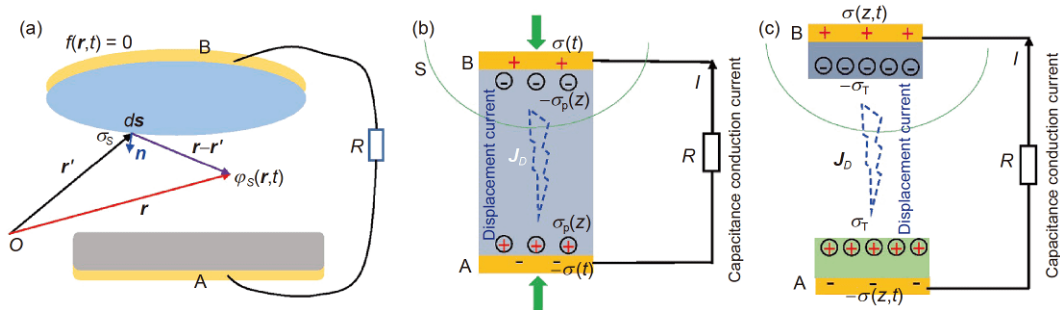


Figure 2 (Color online) (a) Schematic illustration for a nanogenerator connected with a load resistor and its mathematical coordination system; (b) sketch of the internal and external current in a piezoelectric nanogenerator; (c) sketch for a triboelectric nanogenerator with internal displacement current and external capacitive conduction current. Reproduced with permission [30]. Copyright 2020, Elsevier.

Furthermore, the major fundamental science, technologies and practical impacts derived from the two components of the Maxwell's displacement current are shown in Figure 3. The first term $\varepsilon\partial\mathbf{E}/\partial t$ of the displacement current proposed by Maxwell gives the birth of electromagnetic wave theory, and the electromagnetic induction causes the emergence of antenna, radio, telegram, TV, Radar, microwave, wireless communication, and space technology. The electromagnetic unification produces the theory of light, laying the theoretical foundation for the invention of laser and development of photonics. The first component has driven the world development in communication and laser technology in the last century. The second term $\partial\mathbf{P}_s/\partial t$ first proposed by Wang by including the non-electric field induced polarization from mechanical triggering set the foundation for the nanogen-

erators [30]. Adding the $\partial\mathbf{P}_s/\partial t$ term in the displacement current and thus in the Maxwell's equations extends their applications to energy! The nanogenerators are regarded as another important application of Maxwell's equations to energy and sensors after the electromagnetic wave theory and technology. In the future, the "tree" in Figure 3 will grow stronger and stronger, possibly leading to technological innovation and largely impacting the human society.

3 Theoretical calculations from the 3D mathematical model

Based on the Maxwell's equations, there are some theoretical studies carried out for the Maxwell's displacement current

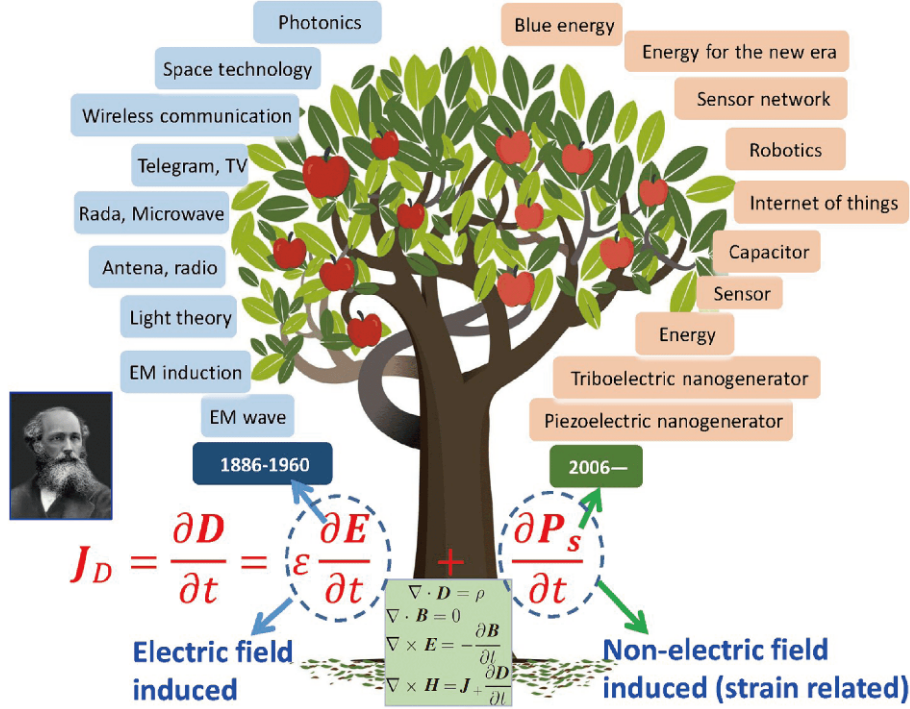


Figure 3 (Color online) Major fundamental science, technologies and practical impacts derived from the two components of the newly revised Maxwell's displacement current. The first term gives the birth of electromagnetic wave theory, having impacted the world development in communication technology in the last century; and the newly added second term gives the birth of nanogenerators, promoting the development of energy technology for the new era, which will impact the world for the future. Reproduced with permission [30]. Copyright 2020, Elsevier.

and the basic output performance of TENGs [31–35]. The displacement current is generated in TENGs due to vertical or horizontal movement of the contacting materials with opposite electrostatic charges. Shao et al. proposed a time-dependent and universal 3D spatial model based on Maxwell's equations to investigate the generation of the displacement current for different TENG mode geometries [31]. To introduce the 3D mathematical model, a Cartesian coordinate system is schematically illustrated in Figure 4(a), which is a right-handed system with base vectors e_x , e_y , and e_z . The vector to a point (x, y, z) from the origin is called as the position vector:

$$\mathbf{e} = xe_x + ye_y + ze_z. \quad (11a)$$

Its magnitude is the distance from the origin:

$$e = \sqrt{x^2 + y^2 + z^2}. \quad (11b)$$

Moreover,

$$\bar{e} = \frac{\mathbf{e}}{e} = \frac{xe_x + ye_y + ze_z}{\sqrt{x^2 + y^2 + z^2}}, \quad (11c)$$

is a unit vector pointing radially outward. A typical differential length at the point (x, y, z) resulting from the differential changes dx , dy and dz is

$$dl = dx\mathbf{e}_x + dy\mathbf{e}_y + dz\mathbf{e}_z. \quad (11d)$$

Using the above Cartesian coordinates, assume we have N finite-sized planes, all with the same geometric dimensions a and b along the x and y directions, respectively. The planes are all centered at $(x, y) = (0, 0)$ and located at positions z_1, \dots, z_N with surface charge densities $\sigma_1, \dots, \sigma_N$, respectively (Figure 4(b)). The electric potential at an arbitrary point $\mathbf{r} = (x, y, z)$ is

$$\phi(x, y, z) = \sum_{i=1}^N \int_{-a/2}^{a/2} \int_{-b/2}^{b/2} \frac{\sigma_i dx' dy'}{4\pi\epsilon(\mathbf{r}) \sqrt{(x-x')^2 + (y-y')^2 + (z-z_i')^2}} = \sum_{i=1}^N \frac{\sigma_i}{4\pi\epsilon(\mathbf{r})} \int_{-a/2}^{a/2} \int_{-b/2}^{b/2} \frac{dx' dy'}{\sqrt{(x-x')^2 + (y-y')^2 + (z-z_i')^2}}, \quad (12a)$$

where $\epsilon(\mathbf{r}) = \epsilon_a$ is the permittivity of the dielectric material a , and the electric field is

$$\mathbf{E}(x, y, z) = -\nabla\phi = \sum_{i=1}^N \frac{\sigma_i}{4\pi\epsilon(\mathbf{r})} \int_{-a/2}^{a/2} \int_{-b/2}^{b/2} \frac{dx' dy'}{\sqrt{(x-x')^2 + (y-y')^2 + (z-z_i')^2}} \frac{(x-x', y-y', z-z_i')}{\sqrt{(x-x')^2 + (y-y')^2 + (z-z_i')^2}}. \quad (12b)$$

Considering the CS mode in Figure 4(c), the electric potentials at $z = z_4$ and $z = z_1$ are given by

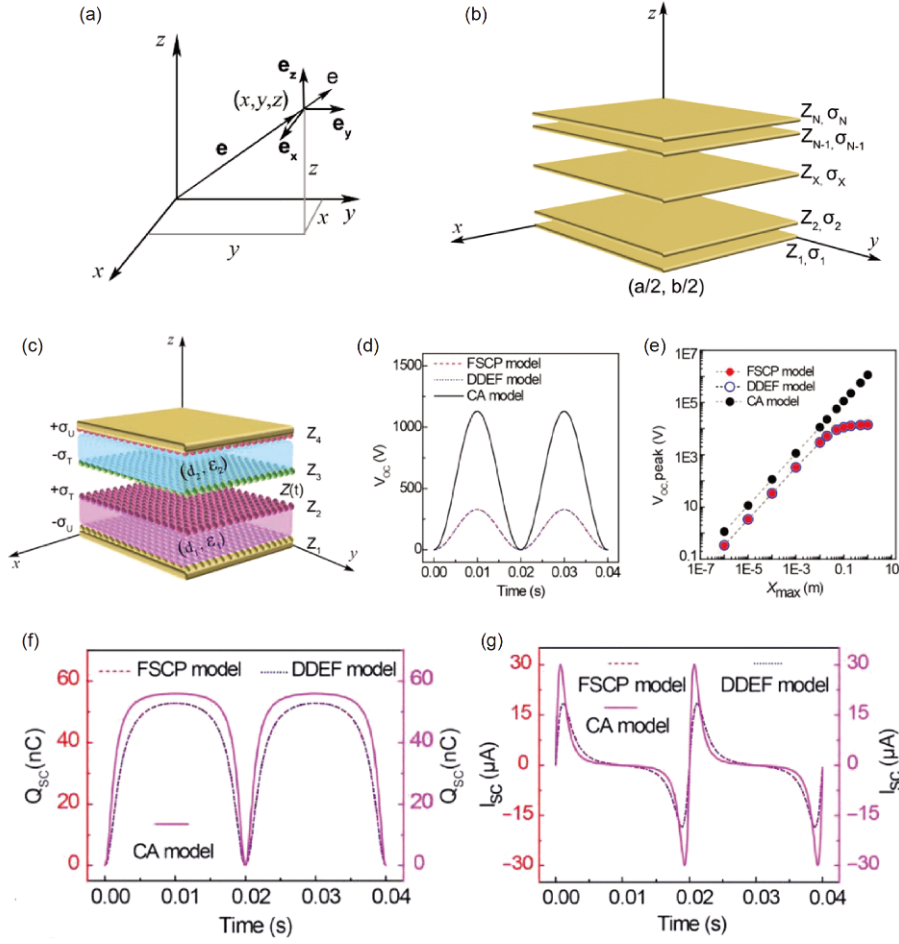


Figure 4 (Color online) (a) Schematic illustration of a Cartesian coordinate system; (b) schematic model of the N finite sized planes located at positions z_1, \dots, z_N with surface charge densities $\sigma_1, \dots, \sigma_N$, constructed in the Cartesian coordinate system; (c) schematic illustration of a typical contact-separation mode TENG in the rectangular coordinate system; (d) comparison of the potential difference at OC conditions (V_{OC}) from the FSCP (or 3D mathematical) model, DDEF model and CA model [31,34,44]; (e) comparison of the peak V_{OC} for different x_{max} from the three different models; (f) comparison of the transferred charges (Q_{SC}) and (g) short-circuit current (I_{SC}) from the three different models at SC conditions. Reproduced with permission [31]. Copyright 2019, Elsevier.

$$\begin{aligned}\phi(0, 0, z_4) &= -\frac{\sigma_u}{\pi\epsilon_2} \int_{z_4-z_1}^{\infty} f(z')dz' + \frac{\sigma_u}{\pi\epsilon_2} \int_0^{\infty} f(z')dz' + \frac{\sigma_T}{\pi\epsilon_2} \int_{z_4-z_2}^{\infty} f(z')dz' - \frac{\sigma_T}{\pi\epsilon_2} \int_{z_4-z_3}^{\infty} f(z')dz', \\ \phi(0, 0, z_1) &= -\frac{\sigma_u}{\pi\epsilon_1} \int_0^{\infty} f(z')dz' + \frac{\sigma_u}{\pi\epsilon_1} \int_{z_1-z_4}^{\infty} f(z')dz' + \frac{\sigma_T}{\pi\epsilon_1} \int_{z_1-z_2}^{\infty} f(z')dz' - \frac{\sigma_T}{\pi\epsilon_1} \int_{z_1-z_3}^{\infty} f(z')dz'.\end{aligned}\quad (13)$$

Assuming an electrical resistance R is connected between the two electrodes, the potential over R is

$$-RA \frac{d\sigma_u}{dt} = \phi(0, 0, z_4) - \phi(0, 0, z_1), \quad (14)$$

where A is the electrode area and σ_u is the charge density. For completeness, the transport equation is written out:

$$\begin{aligned}-RA \frac{d\sigma_u}{dt} &= \frac{\sigma_u}{\pi\epsilon_2} \int_0^{z_4-z_1} f(z')dz' + \frac{\sigma_T}{\pi\epsilon_2} \int_{z_4-z_2}^{z_4-z_3} f(z')dz' \\ &\quad + \frac{\sigma_T}{\pi\epsilon_1} \int_{z_1-z_2}^{z_1-z_3} f(z')dz' + \frac{\sigma_u}{\pi\epsilon_1} \int_0^{z_1-z_4} f(z')dz'.\end{aligned}\quad (15)$$

Note that eq. (15) is a time-dependent differential equation, from which $\sigma_u(t)$ can be evaluated. Then, the conduction current ($I(t)$), instantaneous power ($P(t)$), output energy

($E(t)$), and average power output (P_{av}) can be obtained. While simple, the built 3D mathematical model and computational method are important and applicable to all other types of TENGs despite their different configurations. For instance, comparison of the potential difference (V_{OC}) and the peak V_{OC} at open circuit conditions from the FSCP (or 3D mathematical model) model, distance-dependent electric field (DDEF) [34] model and the capacitance (CA) model are shown in Figure 4(d)–(e), respectively. Figure 4(f)–(g) displays the comparison of the transferred charges (Q_{SC}) and short-circuit current (I_{SC}) from the three different models at short-circuit (SC) conditions. Evidently, the present model and the DDEF model are in exact agreement while the simpler CA model leads to rather different qualitative and

quantitative results. These values as functions of time are considerably larger from the CA model compared to the FCSP (3D mathematical model) and DDEF models. This is mainly because the edge effects are not considered in the formulae, which leads to the large difference especially at a larger maximum moving distance (x_{\max}).

3.1 Theoretical calculations of the Maxwell's displacement current

For a general finite-sized capacitor, the displacement current along the z direction (perpendicular to the capacitor plates) is

$$I_D = \sum_{i=1}^N \int_S dS \frac{\partial}{\partial t} \left(\frac{\sigma_i}{4\pi} \int_{-a/2}^{a/2} \int_{-b/2}^{b/2} dx' dy' \frac{z - z_i}{((x - x')^2 + (y - y')^2 + (z - z_i')^2)^{3/2}} \right). \quad (16)$$

If S extends over the full x - y plane, including the region outside the area defined by the capacitor plates, it is easy to show that I_D is constant in z and given by

$$\begin{aligned} I_D &= \sum_{i=1}^N \int_{-\infty}^{\infty} dx \int_{-\infty}^{\infty} dy \frac{\partial}{\partial t} \left(\frac{\sigma_i}{4\pi} \int_{-a/2}^{a/2} \int_{-b/2}^{b/2} dx' dy' \frac{z - z_i}{((x - x')^2 + (y - y')^2 + (z - z_i')^2)^{3/2}} \right) \\ &= \sum_{i=1}^N \frac{\partial}{\partial t} \left(\frac{\sigma_i}{4\pi} \int_{-a/2}^{a/2} \int_{-b/2}^{b/2} dx' dy' \frac{z - z_i}{((x - x')^2 + (y - y')^2 + (z - z_i')^2)^{3/2}} \right) = ab \sum_{i=1}^N \int_{-\infty}^{\infty} dx_1 \int_{-\infty}^{\infty} dy_1 \frac{\partial}{\partial t} \left(\frac{\sigma_i}{4\pi} \frac{z - z_i}{(x_1^2 + y_1^2 + (z - z_i')^2)^{3/2}} \right). \end{aligned} \quad (17)$$

For the CS model as an example, it has been proven that the displacement current generated in a TENG equals to the conduction current I in the external circuit [31–33], that is

$$I_D = I = \frac{\partial q}{\partial t}. \quad (18)$$

Note that the eq. (18) is essentially similar to the eq. (4) mentioned before. In particular, for CS mode operation (Figure 4(c)), the electric field from the four charged planes can be written as

$$\begin{aligned} E_z(0, 0, z) &= -\frac{\sigma_u}{\pi\epsilon(z)} \arctan \left(\frac{ab}{4(z - z_1) \sqrt{\left(\frac{a}{2}\right)^2 + \left(\frac{b}{2}\right)^2 + (z - z_1)^2}} \right) + \frac{\sigma_T}{\pi\epsilon(z)} \arctan \left(\frac{ab}{4(z - z_2) \sqrt{\left(\frac{a}{2}\right)^2 + \left(\frac{b}{2}\right)^2 + (z - z_2)^2}} \right) \\ &\quad - \frac{\sigma_T}{\pi\epsilon(z)} \arctan \left(\frac{ab}{4(z - z_3) \sqrt{\left(\frac{a}{2}\right)^2 + \left(\frac{b}{2}\right)^2 + (z - z_3)^2}} \right) + \frac{\sigma_u}{\pi\epsilon(z)} \arctan \left(\frac{ab}{4(z - z_4) \sqrt{\left(\frac{a}{2}\right)^2 + \left(\frac{b}{2}\right)^2 + (z - z_4)^2}} \right), \end{aligned} \quad (19)$$

where $\epsilon(z)$ is the permittivity at position z . Hence, $\epsilon(z)$ is a step function depending only on which of the three material layers we evaluate the electric field in. According to the above equations, the numerical results of the displacement current and time-dependent electric field at various loading resistances and maximum contact-separation distances are depicted in Figure 5.

Making further understanding of the displacement current, the established 3D model has also been utilized to evaluate the output performance of the linear sliding (LS) mode TENG [34]. Consider the geometry in Figure 6(a), which is a schematic diagram of a typical dielectric-to-dielectric LS mode TENG in Cartesian coordinates. At the OC conditions, the electric field is written out:

$$\begin{aligned} E(x, y, z, t) &= -\frac{\sigma_T}{4\pi\epsilon(\mathbf{r})} \int_0^{a(t)} dx' \int_{-b/2}^{b/2} \frac{(x - x', y - y', z - z_0^-)}{((x - x')^2 + (y - y')^2 + (z - z_0^-)^2)^{3/2}} dy' + \frac{\sigma_T}{4\pi\epsilon(\mathbf{r})} \int_L^{L+a(t)} dx' \int_{-b/2}^{b/2} \frac{(x - x', y - y', z - z_0^+)}{((x - x')^2 + (y - y')^2 + (z - z_0^+)^2)^{3/2}} dy' \\ &\quad + \frac{\sigma_T}{4\pi\epsilon(\mathbf{r})} \int_0^{a(t)} dx' \int_{-b/2}^{b/2} \frac{(x - x', y - y', z - z_1)}{((x - x')^2 + (y - y')^2 + (z - z_1)^2)^{3/2}} dy' - \frac{\sigma_T}{4\pi\epsilon(\mathbf{r})} \int_L^{L+a(t)} dx' \int_{-b/2}^{b/2} \frac{(x - x', y - y', z - z_2)}{((x - x')^2 + (y - y')^2 + (z - z_2)^2)^{3/2}} dy' \end{aligned}$$

$$+\frac{\sigma_E}{4\pi\epsilon(\mathbf{r})}\int_{a(t)}^L dx' \int_{-b/2}^{b/2} \frac{(x-x', y-y', z-z_1)}{\left((x-x')^2+(y-y')^2+(z-z_1)^2\right)^{3/2}} dy' - \frac{\sigma_E}{4\pi\epsilon(\mathbf{r})}\int_{a(t)}^L dx' \int_{-b/2}^{b/2} \frac{(x-x', y-y', z-z_2)}{\left((x-x')^2+(y-y')^2+(z-z_2)^2\right)^{3/2}} dy', \quad (20)$$

where $a(t)$ represents the relative motion distance and L is the length of the electrode/dielectric. A different charge density $\sigma_E(t)$ ($-\sigma_E(t)$) exists at the overlapping part of the bottom (top) electrode, which is determined by the require-

ment that the total charge σ_0 on the electrodes must be zero at any time. According to the definition, the displacement current through the internal TENG surface z at OC conditions ($I_{D,OC}$) is

$$\begin{aligned} I_{D,OC} &= \int_s \frac{\partial \mathbf{D}}{\partial t} \cdot \mathbf{n} dS = \int_s \frac{\partial D_z}{\partial t} dS \\ &= +\frac{\sigma_T}{4\pi}(z+z_{0^-}) \frac{\partial}{\partial t} \left[\int_{-\infty}^{\infty} dx \int_{-\infty}^{\infty} dy \int_0^{a(t)} dx' \int_{-b/2}^{b/2} \frac{dy'}{\left((x-x')^2+(y-y')^2+(z-z_{0^-})^2\right)^{3/2}} \right] \\ &\quad -\frac{\sigma_T}{4\pi}(z-z_{0^+}) \frac{\partial}{\partial t} \left[\int_{-\infty}^{\infty} dx \int_{-\infty}^{\infty} dy \int_L^{L+a(t)} dx' \int_{-b/2}^{b/2} \frac{dy'}{\left((x-x')^2+(y-y')^2+(z-z_{0^+})^2\right)^{3/2}} \right] \\ &\quad -\frac{\sigma_T}{4\pi}(z-z_1) \frac{\partial}{\partial t} \left[\int_{-\infty}^{\infty} dx \int_{-\infty}^{\infty} dy \int_0^{a(t)} dx' \int_{-b/2}^{b/2} \frac{dy'}{\left((x-x')^2+(y-y')^2+(z-z_1)^2\right)^{3/2}} \right] \\ &\quad +\frac{\sigma_T}{4\pi}(z+z_2) \frac{\partial}{\partial t} \left[\int_{-\infty}^{\infty} dx \int_{-\infty}^{\infty} dy \int_L^{L+a(t)} dx' \int_{-b/2}^{b/2} \frac{dy'}{\left((x-x')^2+(y-y')^2+(z-z_2)^2\right)^{3/2}} \right] \\ &\quad -\frac{1}{4\pi}(z-z_1) \frac{\partial}{\partial t} \left[\sigma_E(t) \int_{-\infty}^{\infty} dx \int_{-\infty}^{\infty} dy \int_{a(t)}^L dx' \int_{-b/2}^{b/2} \frac{dy'}{\left((x-x')^2+(y-y')^2+(z-z_1)^2\right)^{3/2}} \right] \\ &\quad +\frac{1}{4\pi}(z+z_2) \frac{\partial}{\partial t} \left[\sigma_E(t) \int_{-\infty}^{\infty} dx \int_{-\infty}^{\infty} dy \int_{a(t)}^L dx' \int_{-b/2}^{b/2} \frac{dy'}{\left((x-x')^2+(y-y')^2+(z-z_2)^2\right)^{3/2}} \right]. \end{aligned} \quad (21a)$$

When $z = 0$, $I_{D,OC}$ through the triboelectric charge surface is given by

$$I_{D,OC} = b \frac{d\{[L-a(t)]\sigma_E(t)\}}{dt} = b[L-a(t)] \frac{d\sigma_E(t)}{dt} - b\sigma_E(t) \frac{da(t)}{dt}. \quad (21b)$$

For the same reason, the displacement current at SC conditions ($I_{D,SC}$) is derived as

$$\begin{aligned} I_{D,SC} &= \int_s \frac{\partial \mathbf{D}}{\partial t} \cdot \mathbf{n} dS = \int_s \frac{\partial D_z}{\partial t} dS \\ &= -\frac{\sigma_T}{4\pi}(z-z_{0^-}) \frac{\partial}{\partial t} \left[\int_{-\infty}^{\infty} dx \int_{-\infty}^{\infty} dy \int_0^{a(t)} dx' \int_{-b/2}^{b/2} \frac{dy'}{\left((x-x')^2+(y-y')^2+(z-z_{0^-})^2\right)^{3/2}} \right] \\ &\quad +\frac{\sigma_T}{4\pi}(z-z_{0^+}) \frac{\partial}{\partial t} \left[\int_{-\infty}^{\infty} dx \int_{-\infty}^{\infty} dy \int_L^{L+a(t)} dx' \int_{-b/2}^{b/2} \frac{dy'}{\left((x-x')^2+(y-y')^2+(z-z_{0^+})^2\right)^{3/2}} \right] \\ &\quad +\frac{\sigma_T}{4\pi}(z-z_1) \frac{\partial}{\partial t} \left[\int_{-\infty}^{\infty} dx \int_{-\infty}^{\infty} dy \int_0^{a(t)} dx' \int_{-b/2}^{b/2} \frac{dy'}{\left((x-x')^2+(y-y')^2+(z-z_1)^2\right)^{3/2}} \right] \\ &\quad -\frac{\sigma_T}{4\pi}(z-z_2) \frac{\partial}{\partial t} \left[\int_{-\infty}^{\infty} dx \int_{-\infty}^{\infty} dy \int_L^{L+a(t)} dx' \int_{-b/2}^{b/2} \frac{dy'}{\left((x-x')^2+(y-y')^2+(z-z_2)^2\right)^{3/2}} \right] \end{aligned}$$

$$\begin{aligned}
 & -\frac{\sigma_E(z-z_1)}{4\pi} \frac{\partial}{\partial t} \left[\int_{-\infty}^{\infty} dx \int_{-\infty}^{\infty} dy \int_{a(t)}^L dx' \int_{-b/2}^{b/2} \frac{dy'}{\left((x-x')^2 + (y-y')^2 + (z-z_1)^2 \right)^{3/2}} \right] \\
 & +\frac{\sigma_E(z-z_2)}{4\pi} \frac{\partial}{\partial t} \left[\int_{-\infty}^{\infty} dx \int_{-\infty}^{\infty} dy \int_{a(t)}^L dx' \int_{-b/2}^{b/2} \frac{dy'}{\left((x-x')^2 + (y-y')^2 + (z-z_2)^2 \right)^{3/2}} \right] \\
 & +\frac{\sigma_U(z-z_1)}{4\pi} \frac{\partial}{\partial t} \left[\int_{-\infty}^{\infty} dx \int_{-\infty}^{\infty} dy \int_{a(t)}^L dx' \int_{-b/2}^{b/2} \frac{dy'}{\left((x-x')^2 + (y-y')^2 + (z-z_1)^2 \right)^{3/2}} \right] \\
 & -\frac{\sigma_U(z-z_2)}{4\pi} \frac{\partial}{\partial t} \left[\int_{-\infty}^{\infty} dx \int_{-\infty}^{\infty} dy \int_{a(t)}^L dx' \int_{-b/2}^{b/2} \frac{dy'}{\left((x-x')^2 + (y-y')^2 + (z-z_2)^2 \right)^{3/2}} \right], \tag{22a}
 \end{aligned}$$

where $\sigma_U(t)$ stands for the transferred charge density between the two electrodes. As a result, the charge density on the overlapping area is $\sigma_E(t) + \sigma_U(t)$ (z_0^- position), $-\sigma_E(t) - \sigma_U(t)$ (z_0^+ position), respectively. If $z = 0$ is chosen to evaluate, eq. (22a) becomes

$$\begin{aligned}
 I_{D,SC} &= b[\sigma_E(t) - \sigma_U(t)] \frac{da(t)}{dt} \\
 &+ b[L - a(t)] \left[\frac{d\sigma_U(t)}{dt} - \frac{d\sigma_E(t)}{dt} \right]. \tag{22b}
 \end{aligned}$$

Figure 6(b) illustrates the numerical calculations of the

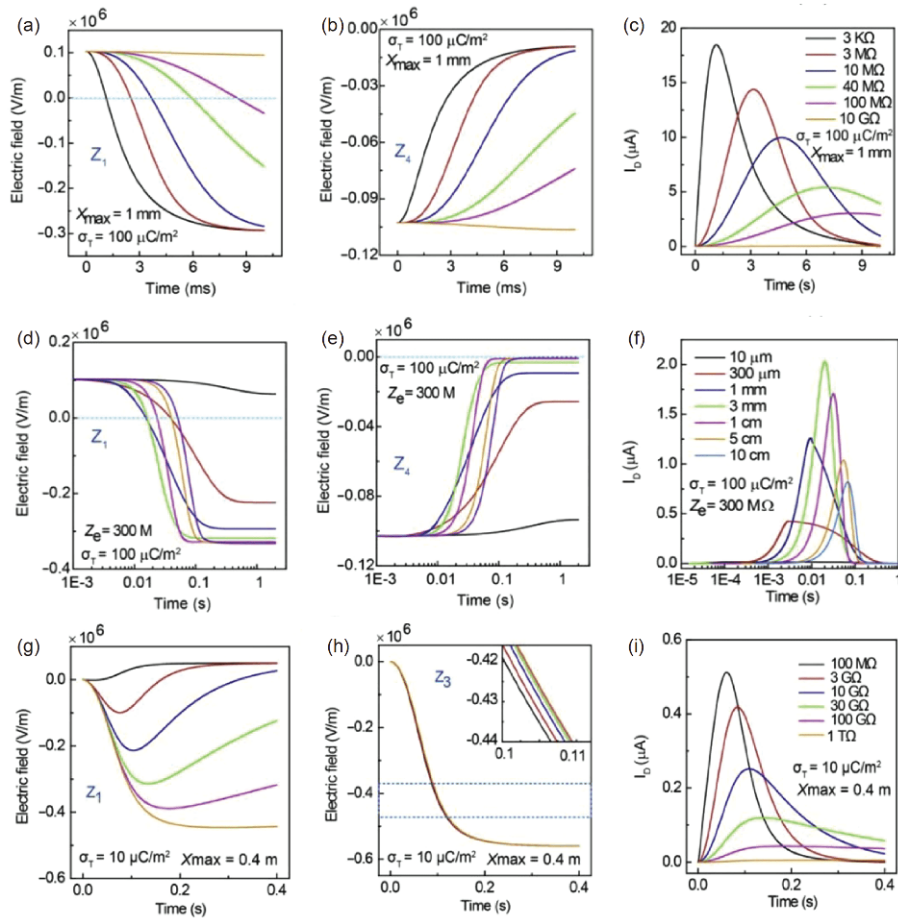


Figure 5 (Color online) Electric field and current characteristics for the contact-separation mode and single-electrode mode TENGs using the present FSCP model. The electric field vs. time at the positions (a, d) z_1 , (b, e) z_4 , and (c, f) the corresponding I_D for different R and x_{max} , respectively. The electric field vs. time at the positions (g) z_1 , (h) z_3 , and (i) the corresponding I_D for different R . Reproduced with permission [31]. Copyright 2019, Elsevier.

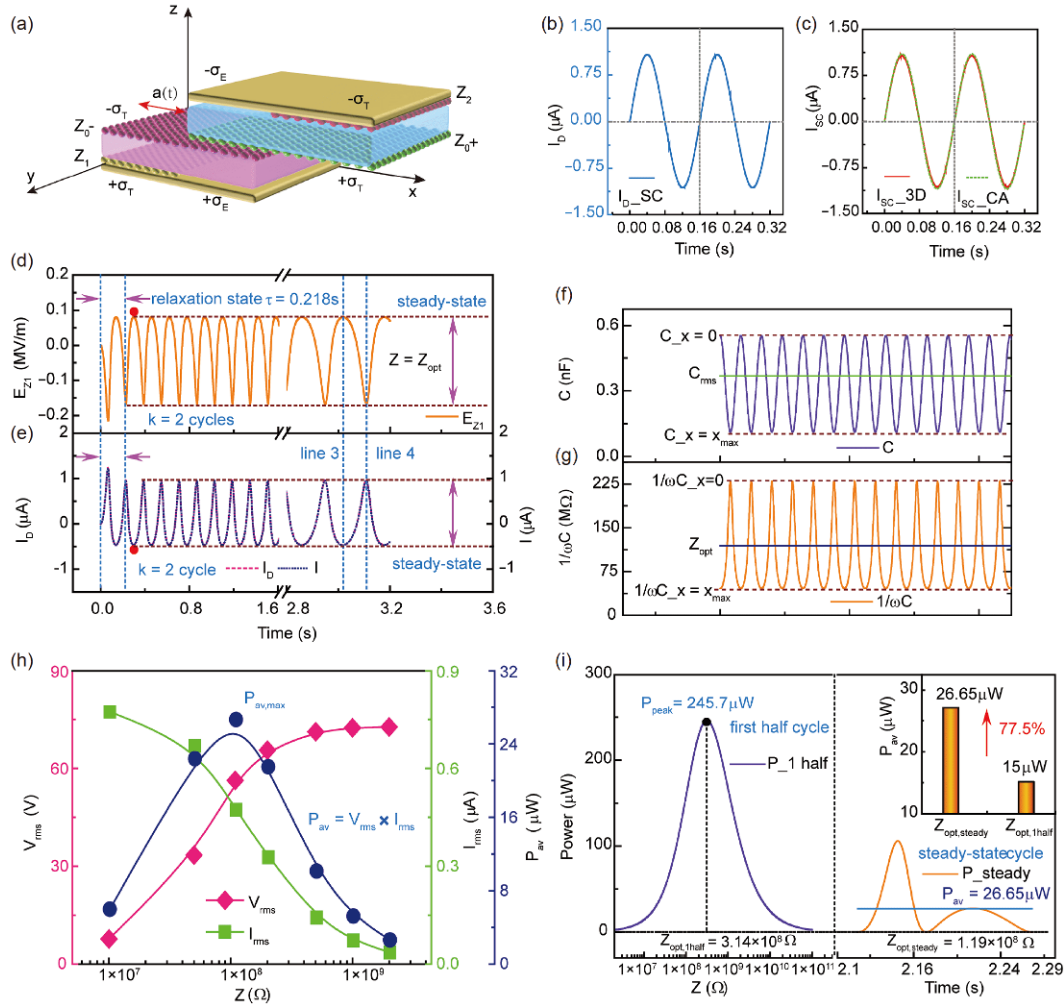


Figure 6 (Color online) (a) Schematic representation of a typical dielectric-to-dielectric LS mode TENG in Cartesian coordinates (3D mathematical model); (b) variation of the displacement current (I_D) at SC condition; (c) comparison of the short circuit current using the 3D model and the capacitance (CA) model; (d) variation of electric field at the z_1 position (bottom electrode) and the corresponding (e) displacement current vs. time under the optimum resistance; (f) capacitance of the LS mode TENG vs. time subject to periodic mechanical motion. Root-mean square capacitance (C_{rms}) calculated from the periodic curve; (g) reactance ($1/\omega C$) of the LS mode TENG vs. time for periodic mechanical motion. The root mean square reactance can be regarded as the optimum resistance (Z_{opt}) of the LS mode TENG at steady state; (h) influence of the load resistance on the equivalent DC value of the voltage (V_{rms}), current (I_{rms}) and average power (P_{av}). Notice that P_{av} is equal to the product of V_{rms} and I_{rms} , and the maximum average power ($P_{av,max}$) can be obtained at Z_{opt} ; (i) comparison of the maximum average power from two different optimum resistances: the first one is from steady state ($Z_{opt,steady}$), and the other is for the first half cycle ($Z_{opt,1half}$) calculated using the same method as before. It can be clearly seen that the $P_{av,max}$ at $Z_{opt,steady}$ is improved by about 77.5% in comparison with that of $Z_{opt,1half}$. Reproduced with permission [33]. Copyright 2020, AIP.

$I_{D,SC}$, the variation of which is identical to that of the current (I_{SC}) at SC conditions. This phenomenon is similar to that of the CS mode, further confirming the conclusion that the displacement current is equal to the conduction current in the external circuit of TENGs. In addition, when a resistor is connected to the electrodes, the $\sigma_U(t)$ can be evaluated from the time-dependent differential equation expressed as eq. (14). The electric field at z_1 position vs. time and relevant displacement current vs. time under the optimum resistance (Z_{opt}) are illustrated in Figure 6(d)–(e), respectively. It can be found that both signals are always parallel and have the same frequency, but change with opposite phase. This is because the generation of displacement current is due to the rate of

change of the electric field. Figure 7(a)–(b) show schematically the variation of electric field for a vertical contact-separation TENG.

On the other hand, in one TENG's charging system that a capacitor acts as the energy storage unit, Shao et al. has demonstrated that the displacement current is indistinguishable from the conduction current I in the external circuit [32]. Its magnitude is proportional to the rate at which the voltage (V^C) across the capacitor varies in time, or, mathematically,
$$I_D = I = C_L \frac{dV^C}{dt}, \quad (23)$$
 where the C_L represents a connected capacitor in external circuit of TENGs. Figure 7(b)–(e) illustrates the real-time I_D

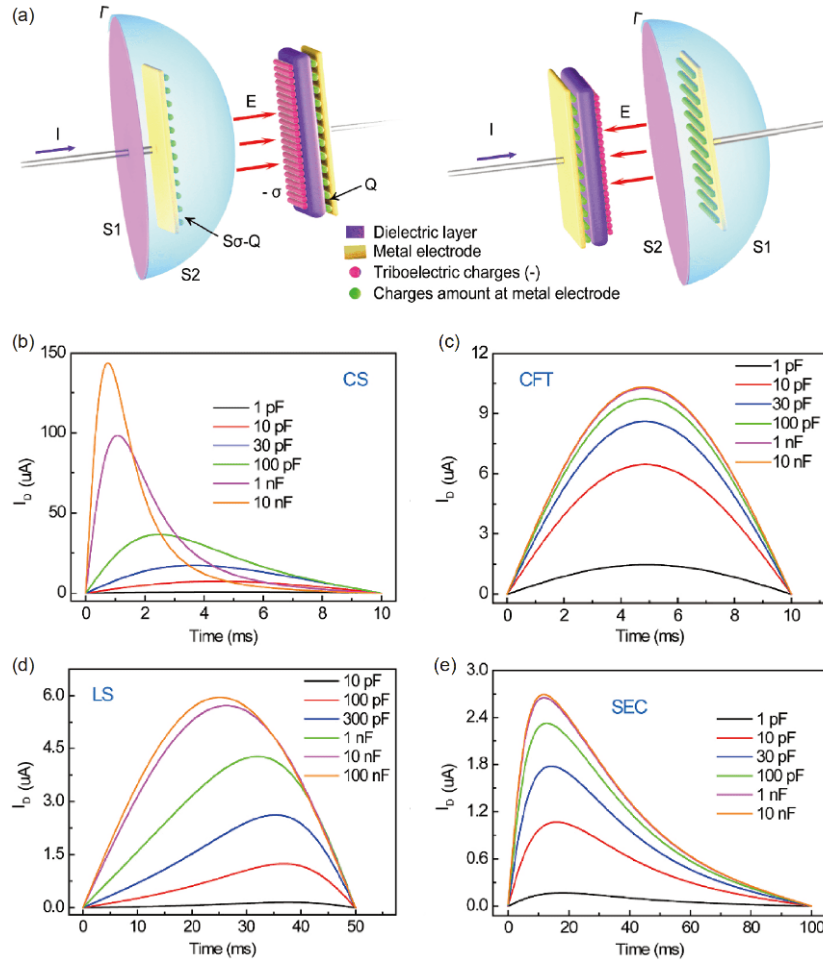


Figure 7 (Color online) Illustrations about the Maxwell's displacement current (I_D) for a vertical contact-separation TENG. (a) Defined surfaces S_1 and S_2 near the metal electrode of the TENG are bounded using a same path Γ . The conduction current I passes through S_1 but not through S_2 , only the displacement current I_D passes through S_2 . The two currents are equal and continuous. Note that the transferred charge between the two electrodes is Q . I_D -time relationships at different load capacitances for (b) contact-separation (CS) mode, (c) contact freestanding triboelectric-layer (CFT) mode, (d) lateral sliding (LS) mode and (e) single-electrode contact (SEC) mode TENGs calculated by analytical formulae. Reproduced with permission [32]. Copyright 2019, Elsevier.

for four basic modes of TENGs under unidirectional mechanical motion with different C_L . It should be noted that a current peak exists for any external C_L , and increasing the C_L increases the maximum I_D for all basic modes of TENGs.

3.2 Theoretical calculations of the conduction current

Except for shedding light on the variation of electric field and the generation of displacement current, the built 3D mathematical model has also been utilized to study the basic characteristics of the alternating current (AC) of TENGs [34]. It has found that a bias voltage equivalent to a direct current (DC) voltage is contained in the basic AC output, giving rise to a large difference between a TENG and the traditional AC power generation system. The root mean square (rms) value of the internal resistance of the TENG ($Z_T(t)$) is regarded as the optimum resistance (Z_{opt}) at steady state, which is defined by

$$Z_{opt} = Z_{rms} = \sqrt{\frac{1}{T} \int_0^T (Z_T(t))^2 dt}, \quad (24)$$

where T represents the period of $Z_T(t)$, and the capacitive reactance of the TENG ($Z_T(t)$) is

$$Z_T(t) \equiv \frac{1}{\omega C(t)} = \frac{1}{2\pi f C(t)}, \quad (25)$$

where ω is the angular velocity, and f is the frequency of the $C(t)$. Under the Z_{opt} a substantial increase (77.5% improvement) is obtained for the average power generation in comparison with the traditional strategy reported for relaxation-time studies. Analytical equations of relaxation and cycle times in steady state are also derived. The relaxation time (τ_{relax}) of a TENG is $\tau_{relax} = 5ZC_{rms}$, where the C_{rms} is written out:

$$C_{rms} = \sqrt{C_{in}^2 + (C_{ac(rms)})^2}. \quad (26)$$

In eq. (26), C_{in} is a fixed value, representing the DC

component or the average value of $C(t)$; $C_{ac(rms)}$ represents the effective value of C_{ac} , which is derived from

$$C_{ac(rms)} = \sqrt{\frac{1}{T} \int_0^T (C_{ac}(t))^2 dt}. \quad (27)$$

For the LS mode TENG as an example, the C_{ac} is $\frac{\epsilon_0 b a_{max}}{2d_0} \cos(\omega t)$, which is a function of time, and T is the period of C_{ac} . The corresponding needed minimum number k_{relax} of cycles is

$$k_{relax} = \frac{\tau_{relax}}{T}, \quad (28)$$

indicating that after k_{relax} cycles the TENG eventually reaches the steady state, resulting in steady power output. In general, the relevant minimum integer N that the TENG can reach in steady state is obtained by $N = \text{Int}(k_{relax})$, implying rounding up the argument to the nearest integer. That is why the minimum cycles shown in Figure 6(d) and 6(e) can be given. Similar to the analysis of the C_{rms} and Z_{rms} , the relationship between the output average power (P_{av}) and the product of V_{rms} and I_{rms} is

$$P_{av} = V_{rms} I_{rms}, \quad (29)$$

where the V_{rms} , I_{rms} represent the *rms*/effective voltage, and current of TENGs, respectively.

Figure 6(f)–(g) demonstrates the numerical calculations of the $C(t)$ and $Z_T(t)$ vs. time subject to periodic mechanical motion, respectively. It is apparent that a DC component is contained in the AC signals. Although the AC plot is not a pure sine/cosine curve, it is periodic with the characteristic frequency of ω . The peaks of V_{rms} , I_{rms} and P_{av} in steady state under different load resistors are plotted in Figure 6(h). As the load resistance increases from small to large, there are three different regions from these profiles, which is in good accordance with previous researches [25]. Furthermore, the P_{av} is equal to the product of V_{rms} and I_{rms} , which is $P_{av} = V_{rms} \times I_{rms}$, as expressed in eq. (29). And the maximum P_{av} can be found around the $1.19 \times 10^8 \Omega$, the value of which is equal to the result calculated by eq. (24), offering a direct evidence for the prediction that the *rms* value of $Z_T(t)$ can be regarded as the optimum resistance of TENGs. Under the optimum resistance in steady state ($Z_{opt,steady}$), the numerical calculated P_{av} is about $26.65 \mu\text{W}$, which is improved by a factor of 77.5% when compared to that at the optimum resistance calculated for the first half cycle ($Z_{opt,1half}$) (Figure 6(i)). So, the optimum resistance of a TENG system is more appropriately obtained using the effective value of $Z_T(t)$ rather than from the first half cycle/the relaxation state.

4 Theoretical calculations from the capacitor models

Besides the theoretical researches starting from the Max-

well's equations, there are more theoretical works about the performance predictions of TENGs through the traditional parallel-plate capacitor models [36–43]. Before the theoretical foundation of TENGs was proved to be the Maxwell's displacement current in 2017, all the theoretical calculations are based on the capacitor model. The key of those calculations is to obtain the governing equation of TENGs using the capacitor model, i.e., V - Q - x relationship [44]. The TENG can be equivalent to a serial connection of an ideal voltage source and a capacitor, so the governing differential equation can be given by

$$V = -\frac{Q}{C(x)} + V_{oc}(x), \quad (30)$$

where the $V_{oc}(x)$ and $C(x)$ relationships can be usually obtained numerically through finite-element simulations together with continuous fraction interpolation method, or derived analytically for certain mode TENGs with appropriate approximations. The real-time dynamic output characteristics of TENGs can be calculated numerically or analytically by solving the differential eq. (30) under specified TENG mode and motion conditions. In this section, we will introduce the progress of the theoretical calculations on the TENG performance using the traditional parallel-plate capacitor model and edge approximation based equivalent capacitance (EDAEC) model.

4.1 Traditional parallel-plate capacitor model

Niu et al. have done systematic studies on the output characteristics of four basic modes of TENGs based on the traditional parallel-plate capacitor models [25–28]. For the first working mode, i.e., the contact-separation mode [25], the theoretical models of the TENG constructed for the dielectric-to-dielectric attached-electrode and conductor-to-dielectric attached-electrode cases are schematically shown in Figure 8(a)–(b). In the dielectric-to-dielectric attached-electrode mode, two dielectric plates attached by two metal electrodes on their back faces are located face to face. Their thicknesses and relative dielectric constants are represented by d_1 , d_2 , ϵ_{r1} , ϵ_{r2} , and their separation distance is defined by $x(t)$. Under an external mechanical force, the separation distance x can be varied, and a potential difference (V) between the two electrodes will be induced. The transferred charge amount driven by the induced potential difference is represented by Q . For the conductor-to-dielectric attached-electrode mode in Figure 8(b), the Metal 1 serves as not only the electrode, but also the triboelectric layer contacting and separating with the Dielectric 2. The equivalent capacitor model of the conductor-to-dielectric mode is presented in Figure 8(c), indicating that the Metal 1, Metal 2, and the whole Dielectric 2 surface can be respectively thought as Node 1, Node 3, and Node 2 in such electrostatic system,

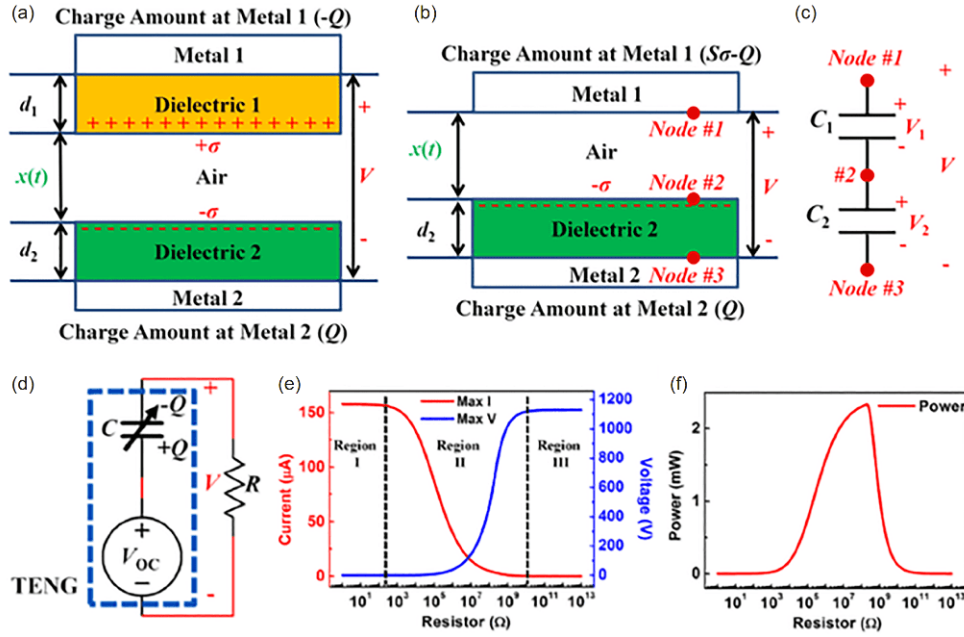


Figure 8 (Color online) (a)–(b) Theoretical models for a contact-mode TENG based on the parallel-plate capacitors: (a) dielectric-to-dielectric attached-electrode mode, and (b) conductor-to-dielectric attached-electrode mode; (c) equivalent capacitor model for the conductor-to-dielectric attached-electrode TENG; (d) equivalent circuit model for the contact-mode TENG; (e) calculated output current and voltage with respect to the load resistance with the three working regions marked; (f) dependence of the instantaneous output power on the load resistance. Reproduced with permission [25]. Copyright 2015, Elsevier.

based on the assumption of the infinitely large and uniform surface of Dielectric 2. Equivalent capacitances are formed between the Node 1 and Node 2 and between the Node 2 and Node 3, while the capacitance between the Node 1 and Node 3 does not exist, because the electrical line connection of Node 1 and Node 3 is fully blocked by the Node 2.

By applying the infinitely-large parallel-plate capacitor model, the governing equation and basic output characteristics for the contact-mode TENG can be derived as

$$V = -\frac{Q}{S\epsilon_0}(d_0 + x(t)) + \frac{\sigma x(t)}{\epsilon_0}, \quad (31)$$

$$V_{OC} = \frac{\sigma x(t)}{\epsilon_0}, \quad Q_{SC} = \frac{S\sigma x(t)}{d_0 + x(t)}, \quad C = \frac{\epsilon_0 S}{d_0 + x(t)}, \quad (32)$$

where σ is the surface charge density, S is the tribo-surface area, and d_0 is the effective dielectric thickness defined as the summation of all dielectric thicknesses divided by their relative dielectric constants. When loading a resistor in the external circuit for the contact-mode TENG, by solving the governing eq. (31) under the boundary condition $Q(t=0) = 0$, combining with the Ohm's law, the dynamic output characteristics of the TENG can be calculated as follows:

$$Q(t) = \frac{1}{R} \exp\left[-\frac{1}{R} \int_0^t \frac{dt}{C(x(t))}\right] \int_0^t V_{OC}(x(t)) \times \exp\left[\frac{1}{R} \int_0^t \frac{dt}{C(x(t))}\right] dt, \quad (33a)$$

$$I(t) = \frac{V_{OC}}{R} - \frac{1}{R^2 C} \exp\left[-\frac{1}{R} \int_0^t \frac{dt}{C(x(t))}\right] \int_0^t V_{OC}(x(t)) \times \exp\left[\frac{1}{R} \int_0^t \frac{dt}{C(x(t))}\right] dt, \quad (33b)$$

$$V(t) = V_{OC} - \frac{1}{RC} \exp\left[-\frac{1}{R} \int_0^t \frac{dt}{C(x(t))}\right] \int_0^t V_{OC}(x(t)) \times \exp\left[\frac{1}{R} \int_0^t \frac{dt}{C(x(t))}\right] dt. \quad (33c)$$

The equivalent circuit model for the contact-mode TENG connected with a resistor is shown in Figure 8(d), and the corresponding three-working-region behavior is typically presented in Figure 8(e). As can be seen, the peak current first has little drop in low resistance region (Region I), and then decreases (Region II), and finally gets saturated in Region III. The peak voltage exhibits similar three-working-region behavior, which increases to a saturated value close to the open-circuit voltage V_{OC} in Region III. Figure 8(f) shows the peak power as a function of the load resistance, indicating that there exists an optimum resistance for the TENG to reach the maximum peak power. This is the general feature of a TENG.

Besides the contact-separation mode TENG, a theoretical model of a lateral-sliding TENG was established by Niu et al. [26]. The finite-element simulations were applied to calculate the basic output characteristics, including the V_{OC} , Q_{SC} , and C at various sliding distances x . Since the length l of the

dielectrics is much larger than their thicknesses d_1 and d_2 , and x is usually smaller than $0.9l$, when neglecting the edge effect, an approximate analytical governing equation can be derived as

$$V = -\frac{d_0}{w\epsilon_0(l-x)}Q + \frac{\sigma d_0 x}{\epsilon_0(l-x)}, \quad (34)$$

where w is the width of the dielectrics, and d_0 is the effective dielectric thickness. Based on the analytical V - Q - x equation, the dynamic output characteristics of the sliding-mode TENG were calculated for any load resistance, showing good agreement with the experimental results.

Similarly, the theoretical models for the single-electrode mode and freestanding mode TENGs have been built to reveal their resistive load characteristics [27,28]. The two types of TENGs also have the contact-mode and sliding-mode. A common characteristic for the single-electrode TENG, contact-mode freestanding TENG, and sliding-mode dielectric-freestanding TENG is that the total capacitance of TENG is nearly constant due to the fixed electrodes. However, the capacitance for the sliding-mode metal-freestanding TENG is varied with the sliding distance, ascribed to the shielding effect of the top metal layer. For a single-electrode TENG, the transferred charges under the short-circuit condition are only half of the tribo-charges, so the maximum charge transfer efficiency is only 50%, relative to the paired-electrode TENG. The $V_{OC}(x)$ equation and the capacitance C_0 for the single-electrode TENG can be obtained by the interpolation method based on the finite-element simulation results, and then the governing equation can be easily solved numerically. The output performance of the single-electrode TENG dependent on the electrode gap and area size were theoretically investigated, showing an optimized electrode gap distance and an optimized area size for maximizing the output power.

For a contact-mode freestanding TENG, when assuming that the area size is infinitely large and the edge effect can be ignored, since the electrode size is always much larger than the air gap, the V - Q - x equation can be obtained by

$$V = -\frac{d_0+g}{\epsilon_0 S}Q + \frac{2\sigma x}{\epsilon_0}, \quad (35)$$

where g is the total air gap between two metal plates. Compared to a contact-separation TENG, the V_{OC} and Q_{SC} of such TENG both exhibit linear relationships with the separation distance x due to the constant capacitance. On the other hand, the sliding-mode freestanding TENG has different output performances, determined by the material type of the freestanding layer. The real-time dynamic output characteristics with respect to the structural parameters were also studied through the numerical method to improve the TENG structure and performance.

To provide the further optimization solution for the TENG performance, Niu et al. constructed theoretical models of

grating structured TENGs [36], which can produce efficient charge transfer due to the increase in the charge separation cycle. Such TENGs can also realize a higher output current and lower matched resistance. The output characteristics of the TENGs were compared for two grating structured TENGs with equal plate-length and with unequal plate-length, where the calculations adopt the initial boundary condition and periodic boundary condition, respectively. For the two cases, increasing the grating number to get a finer pitch can generally improve the outputs, but a too fine pitch can produce obvious edge effect. Therefore, an optimum grating number and an optimum unit aspect ratio exist. For the unequal plate-length case, the dielectric thickness of the longer plate needs to be much smaller than that of the shorter plate. Additionally, Jiang et al. carried on simulations and numerical or analytical calculations to investigate the output performance of a rotary freestanding TENG with grating structure [39], as well as a rotary-sliding disk TENG [40]. The influences of the structural parameters and external operation conditions were detailedly addressed. These theoretical studies are useful for deepening the understanding of the working principle of the grating structured TENGs, and provides guidelines for rational design of TENG structures toward the maximum electric outputs.

4.2 Edge approximation based equivalent capacitance model

The above discussed theoretical works are based on the traditional parallel-plate capacitor model, where the edge effects are mostly ignored. Actually, the edge effect of the capacitance cannot be ignored for specific TENG structures such as the lateral-sliding TENG and sliding-mode freestanding TENG. For instance, the short-circuit transferred charge and open-circuit voltage of the sliding-mode freestanding TENG do not change linearly with the sliding distance due to the edge effect. A universal EDAEC model was recently proposed by Zi et al. to demonstrate the charge distributions and electric field in all modes of TENGs [45], with consideration of the capacitances created by the edge effects. Figure 9(a)–(b) shows the sketches of the traditional and EDAEC models for a lateral-sliding TENG. In the traditional model, the total capacitance C_{total} is dominated by the capacitance at the overlapped region between electrodes 1 and 2, which can be calculated by

$$C_{total} = \frac{\epsilon_r \epsilon_0 (L-x)w}{\epsilon_r d + d_0}, \quad (36)$$

where w is the width of the dielectrics and ϵ_r is its relative dielectric constant. The equivalent capacitance of C_{total} can be described as the series connection of C_{b1} and C_{b2} , which are the capacitances between the surface b and two electrodes. However, in the EDAEC model, the equivalent capa-

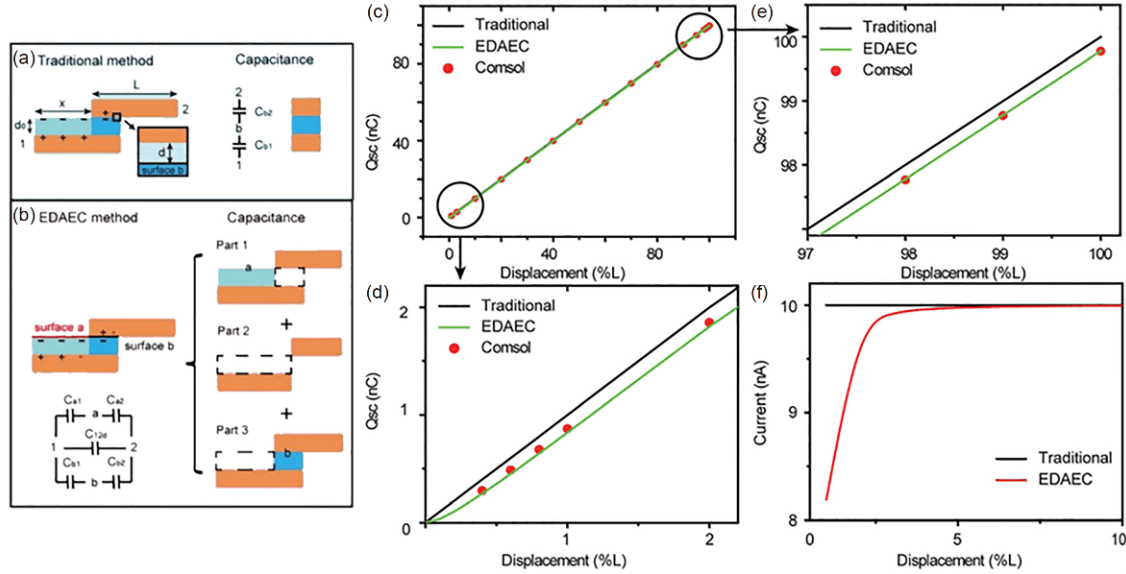


Figure 9 (Color online) (a)–(b) Schematic illustrations of the charge distributions and equivalent capacitor models for a lateral-sliding TENG when using different methods: (a) traditional method; (b) EDAEC method; (c)–(e) comparison of short-circuit transferred charge Q_{SC} obtained by the traditional, EDAEC methods, and COMSOL simulations; (f) comparison of short-circuit current obtained by the traditional and EDAEC methods. Reproduced with permission [45]. Copyright 2019, Royal Society of Chemistry.

capacitance of C_{total} consists of three parts: series capacitance C_{1a2} of edge capacitances C_{a1} and C_{a2} between surface a and two electrodes; edge capacitance C_{12d} between two electrodes; series capacitance C_{1b2} of C_{b1} and C_{b2} at the overlapped region. Therefore, the total capacitance can be obtained by

$$C_{total} = C_{1a2} + C_{12d} + C_{1b2} = \frac{\varepsilon_r \varepsilon_0 x w \times C_a}{\varepsilon_r \varepsilon_0 x w + C_a d_0} + C_{12d} + \frac{\varepsilon_r \varepsilon_0 (L-x) w}{\varepsilon_r d + d_0}, \quad (37)$$

where C_a is the value of the C_{a2} and is a small constant. According to the capacitance equations and the charge superposition principle, the short-circuit charge, current and open-circuit voltage were calculated.

Figure 9(c)–(e) shows the transferred charge Q_{SC} calculated by various models and the COMSOL simulations and local enlarged views. It can be found that Q_{SC} from the traditional model changes linearly with the distance x , while the Q_{SC} - x curve from the EDAEC model is not strictly linear, exhibiting a flatter start at the beginning, and then an increased slope until the same with that from the traditional model. Obviously, the calculation results from the EDAEC model are more consistent with the simulation results than the traditional model. Figure 9(f) provides the profiles of the current with respect to x from the two models at a constant sliding speed based on the Q_{SC} results. The current obtained from the EDAEC model is much lower at smaller x , and then increases rapidly, while the current from the traditional model is constant, verifying the reasonability of the EDAEC model. Similarly, this model is more suitable for the calculations of the voltage and capacitance. In addition, the ana-

lytical models and quantitative Q - V - x relationship were also established for other TENG modes through the universal EDAEC method, providing in-depth understanding of the working principles of different TENGs toward efficient energy harvesting.

5 Figure-of-merits and standards of TENGs

Due to the rapid development of the TENG technology, a universal standard is necessary to evaluate/quantify the performance of TENGs, regardless of the structure and operation mode. The establishment of the standards will set the foundation for the further applications and industrialization of the TENGs. Recently, Prof. Wang's group has proposed a standard method to quantitatively evaluate the TENG performance from points of view of both the structure and materials through constructing the cycles for maximized energy output (CMEO) of TENG [46]. In this section, we mainly introduce the definition of performance figure-of-merits of TENGs as the standards of TENGs, and the progress of calculations for the figure-of-merits in different cases.

5.1 Performance figure-of-merits and standards of TENGs

Zi et al. investigated the output energy per cycle for TENG starting from the V - Q curve, and first proposed the cycles for maximized energy output of the TENG [46]. Based on such

cycles, according to the average output power and energy conversion efficiency of TENG, a performance figure-of-merit (FOM_P) was proposed as the standard for quantifying the performance of TENG, including a structural figure-of-merit (FOM_S) related with the TENG design and a material figure-of-merit (FOM_M) equal to the square of the surface charge density. Taking the lateral-sliding TENG for instance, the schematic diagram for the TENG structure and the CMEO at a certain resistance are shown in Figure 10(a)–(b). The key to realize the maximized energy per cycle is to increase the maximum cycling charge Q_C up to the maximum short-circuit charge $Q_{SC,max}$ by a four-step method using a switch in parallel with the resistor. In step 1, at switch off, the top tribo-layer slides from $x = 0$ to $x = x_{max}$; in step 2, turn on the switch to achieve instantaneous short-circuit condition and then turn off the switch; in step 3, the top tribo-layer slides back to the initial position at switch off; in step 4, turn on the switch again, and then turn off it. The CMEO curves for different load resistances were also calculated as shown in Figure 10(c). It can be seen that when the resistance increases to be infinitely large, the V - Q curve becomes into a trapezoid shape with the largest encircled area. Then the largest possible output energy per cycle E_m can be theoretically calculated by

$$E_m = \frac{1}{2} Q_{SC,max} (V_{OC,max} + V'_{max}), \quad (38)$$

where the maximum open-circuit voltage $V_{OC,max}$, maximum short-circuit charge $Q_{SC,max}$, and maximum achievable absolute voltage V'_{max} at $Q = Q_{SC,max}$ determine the trapezoid vertices.

The dimensional structural figure-of-merit FOM_S of

TENG was defined as

$$FOM_S = \frac{2\varepsilon_0 E_m}{\sigma^2 A x_{max}}, \quad (39)$$

and then the performance figure-of-merit FOM_P was defined as

$$FOM_P = FOM_S \cdot \sigma^2 = 2\varepsilon_0 \frac{E_m}{A x_{max}}, \quad (40)$$

where the σ^2 is the FOM_M . The FOM_P is proportional to the largest possible average output power and associated with the highest achievable energy conversion efficiency, regardless of the TENG mode, structure and size, so it can be regarded as the standard of TENGs. Zi et al. calculated the FOM_S through the analytical formulae and finite-element simulations for different TENG modes and compared them as shown in Figure 10(d). The freestanding configuration was found to have the highest FOM_S due to the lower capacitance between the electrodes. The FOM_S of paired-electrode TENG is higher than that of single-electrode TENG, because the transferred charge and built-in voltage are suppressed in the single-electrode TENG. Besides four basic modes of TENGs, Jiang et al. studied the output characteristics of rolling freestanding TENG and calculated the structural figure-of-merits [47]. The results indicated that the average output power of rolling freestanding TENG could be optimized by maximizing the FOM_S , which is dependent on the structural parameters.

For measuring surface charge density σ to obtain the material figure-of-merit FOM_M of TENG, Zi et al. set up an experiment equipment by using the liquid metal as one electrode, and the Cu film attached by the test material as another electrode, as schematically shown in Figure 10(e).

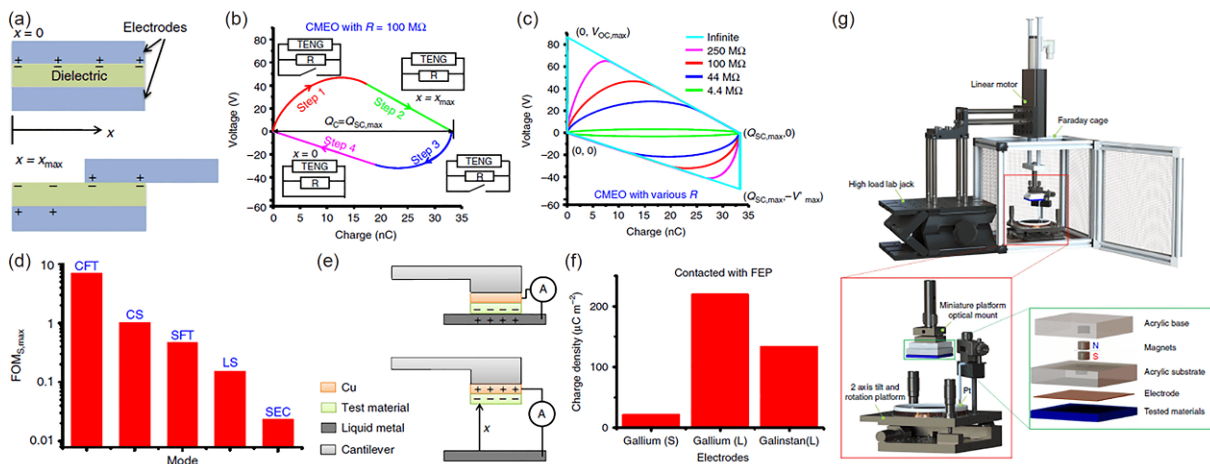


Figure 10 (Color online) (a) Schematic structure of a lateral-sliding mode TENG at the displacement $x = 0$ and $x = x_{max}$; (b) voltage-charge plot at a load resistance of 100 MΩ showing the four steps for realizing the cycle for maximized energy output (CMEO) of TENG through the opening and closing of the switch as shown in the insets. The maximum cycling charge Q_C reaches the maximum short-circuit charge $Q_{SC,max}$; (c) the CMEO at various load resistances, where the vertices of the CMEO for infinitely-large resistance are marked; (d) comparison of the maximum structural FOM for different TENG modes calculated from the finite element method; (e) schematic diagram of the equipment for charge density measurement on the test material surface by using liquid metal as one electrode; (f) comparison of the measured surface charge density of FEP film by contacting it with solid gallium, liquid gallium and galinstan. Reproduced with permission [46]. Copyright 2015, Macmillan Publishers Limited; (g) schematic diagram of the experimental set-up for the measurements of triboelectric series. Reproduced with permission [48]. Copyright 2019, Springer Nature.

The electrification occurs between the test material and the liquid metal, and the transferred charges under the short-circuit condition are approximately equivalent to the tribo-charges when the test material is lifted above the liquid metal for a height much larger than the material thickness. So the surface charge density σ can be calculated by the measured transferred charges divided by the tribo-surface area. Figure 10(f) presents the results of the measured charge density σ on the fluorinated ethylene propylene (FEP) surface by contacting it with solid gallium, liquid gallium and galinstan. The liquid metal can have better contact intimacy with the material than the solid metal, leading to higher measured σ . The triboelectric performances of different materials were quantified by the σ with respect to the liquid galinstan. Taking the σ when contacting FEP with galinstan as the reference, a dimensionless material FOM (FOM_{DM}) for triboelectrification was defined as

$$\text{FOM}_{\text{DM}} = \frac{\sigma_{\text{Material/Galinstan}}^2}{\sigma_{\text{FEP/Galinstan}}^2}. \quad (41)$$

Furthermore, Zou et al. proposed a universal standard method to quantify the triboelectric series for a wide range of polymer materials [48], and standardized the experimental set-up, as shown in Figure 10(g). The triboelectric charge density (TECD) was quantitatively measured in a glove box under well-controlled conditions, with fixed temperature, pressure and humidity. By the standard experimental set-up and measurement method, the quantified triboelectric series were obtained as shown in Figure 11. The TECD of a 20 mil-thick polytetrafluoroethylene (PTFE) was used as the reference to reflect the normalized TECD of dozens of materials. This quantified triboelectric series will serve as a textbook standard for implementing the applications of triboelectrification for energy harvesting and self-powered sensing.

5.2 Structural figure-of-merits of TENGs at powering loads

Structural figure-of-merit is a very useful technique to evaluate and compare the output performance of TENGs, but it is still limited in some way. Because its largest possible output energy E_m is calculated by the product of open-circuit voltage (V_{OC}) and short-circuit charges (Q_{SC}), which is significantly larger than that of the situation when TENG is connected with an external load. In other words, it can't be utilized to compare the real output power of TENGs under different load resistances. Therefore, Shao et al. proposed an improved and operable route to getting the actual maximum harvesting energy (E_m) [49].

For the LS mode TNEG as an example demonstrated in Figure 12(a), four working steps can be divided in one operation cycle. For the step I, as the sliding part moves from x

$= 0$ to $x = x_{\text{max}}$, some charges flow from the top electrode to the stationary one to balance the potential difference, which is called as the triboelectric process. For the step II, when the move part stops at x_{max} and charges are transferred to the bottom electrode continuously until the potential difference is 0; this is strongly different from the assumption proposed by Zi et al. in which a switch is needed to be turned on/off. The change in step II is very much like a zero input response in a conventional RC circuit, so that this step can be called the transient process. The time needed in this process largely relies on the product by the load resistance and capacitance of the TENG at x_{max} . Therefore, the half cycle of TENGs is divided into two processes: triboelectric process and transient process. As a result, in one whole operation cycle the steps I and III belong to the triboelectric process, while the transient process contains the steps II and IV. Because each step can be described by a first-order differential equation, four different governing equations are derived in one cycle. After solving these four equations, the power output ($P(t)$) in a corresponding step is obtained, thus the practical and total energy is equal to the integral of power to the time, which is defined as

$$E_m = \int_0^{t_1} P_1(t)dt + \int_{t_1}^{t_2} P_2(t)dt + \int_{t_2}^{t_3} P_3(t)dt + \int_{t_3}^{t_4} P_4(t)dt, \quad (42)$$

where P_1 , P_2 , P_3 and P_4 stand for the instantaneous power at steps I, II, III, and IV, respectively. Through this method, the maximum harvested energy and structural figure-of-merit with different load resistances (FOM_{RS}) have been clearly investigated. During these different external loads, what we pay the most attention to is the optimum resistance, under which the mechanical energy can be more effectively converted into electric power, and the related E_m and FOM_{RS} are more practical in comparison with other resistances. The FOM_{RS} calculated from the optimum load at various x_{max} for four basic modes of TENG are numerically calculated, and compared with the maximum FOMs, as shown in Figure 12 (c)–(f). Although the FOM_{RS} under optimum loads are always smaller than the FOMs for all different kinds of TENGs, they can demonstrate the real output power rather than the possible largest energy of TENGs, providing powerful references for engineering application and designing of TENGs.

5.3 Structural figure-of-merits of TENGs in a charging system

Figure-of-merits of TENGs at powering loads have been established, which can be utilized as the standard to evaluate and compare the energy output of TENGs with different configurations and operation conditions. However, we draw less attention to the TENG's charging characteristics. Shao et al. demonstrated a comprehensive analysis of the funda-

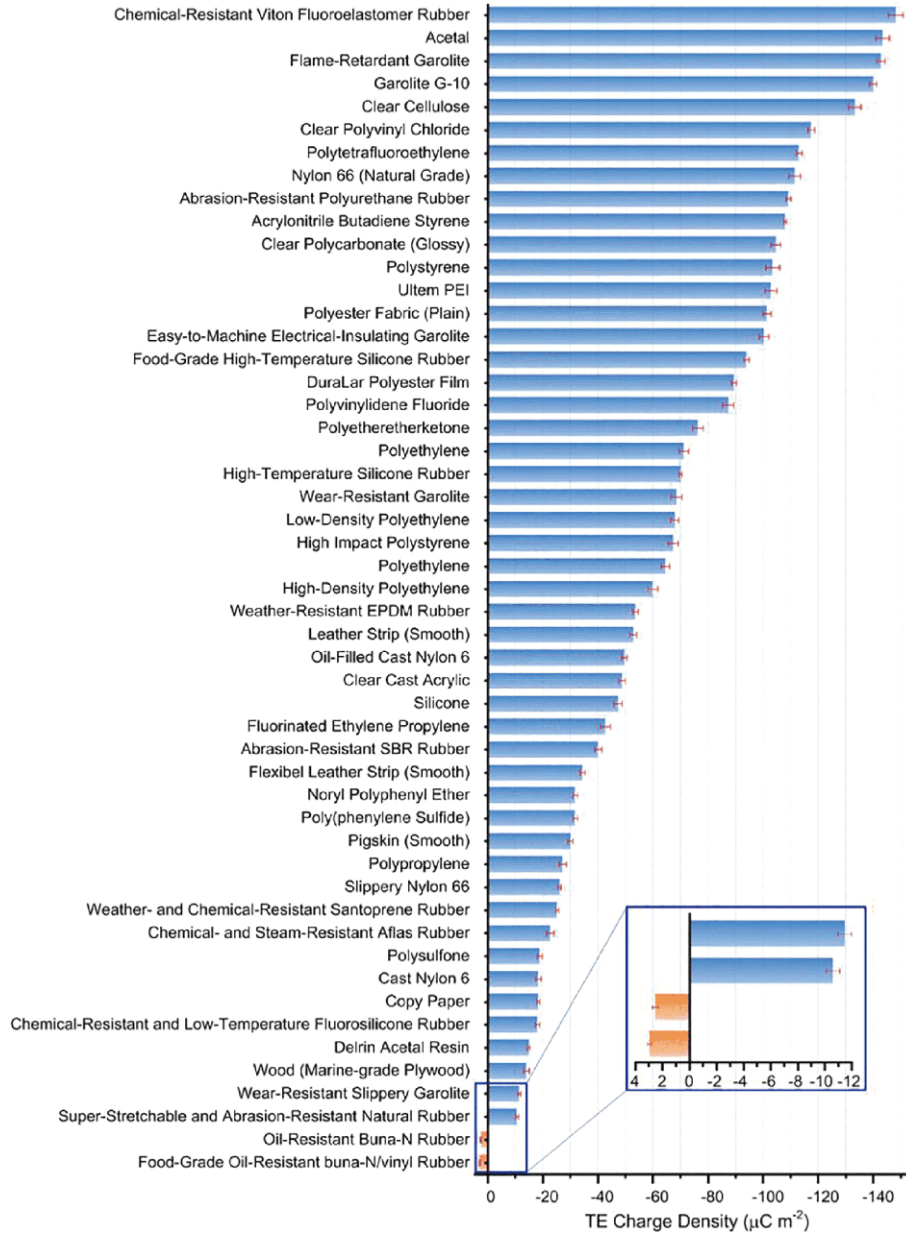


Figure 11 (Color online) Quantified triboelectric series obtained by the standard measurement method and experimental set-up. Reproduced with permission [48]. Copyright 2019, Springer Nature.

mental charging behaviors of TENG [32]. And the structural figure-of-merit of TENGs in a charging system ($FOMC_S$) is proposed, being used as a standard to quantify and predict the TENG's charging performances.

When a capacitor (C_L) is connected in the external circuit of TENGs, its equivalent circuit model is similar to that in Figure 8(d) when its resistor R is replaced by the C_L . It has been proven that the maximum energy E_m^C stored in C_L mainly depends on the final charging cycle numbers k and the saturation voltage V_{sat} of the C_L . In addition, the E_m^C is strongly affected by the area of the tribo-charged surfaces (A), maximum relative distance (x_{max}) as well as the surface charge density (σ). So that to quantitatively evaluate each TENG's

unique charging performance, the structural figure-of-merit in a TENG charging system ($FOMC_S$) is defined as

$$FOMC_S = \frac{2\varepsilon_0 E_m^C}{\sigma^2 kAx_{max}}, \quad (43)$$

where ε_0 is the permittivity of the vacuum. The E_m^C can be calculated by the equation of $V_{sat} = Q_{SC,max} / (C_{min} + C_{max})$. $Q_{SC,max}$ represents the maximum short-circuit transferred charge, while C_{min} and C_{max} stand for the minimum and maximum capacitances of the TENG, respectively. In particular, the E_m^C can also be calculated by the summation of the integral of instantaneous power to the time.

The numerical calculations of the $FOMC_S$ for the four

basic modes of TENGs are depicted in Figure 13. Firstly, it can be found that the structural FOM_S almost have a similar trend compared with the FOM_S (Figure 12(c)–(f)) under the same conditions, but the former are lower as can be seen clearly from the extracted maximum values shown in Figure

7(e). This is due to the available E_m^C stored in C_L is usually smaller than the ideal E_m . Moreover, the charging performance of TENGs driven by the vertical motion (for instance, the CS mode) is better than that of the lateral sliding motion (LS mode). This is because the LS mode TENG has a larger

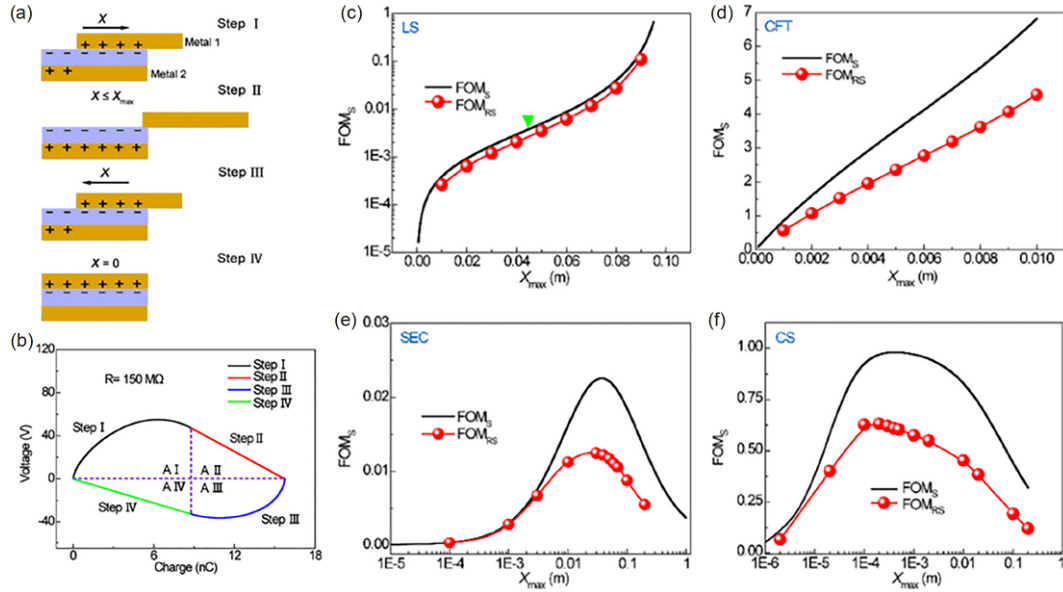


Figure 12 (Color online) (a) Schematic diagram of a lateral sliding (LS) TENG with four steps. Step I, the sliding part moves from $x = 0$ to $x = x_{\max}$; step II, the sliding part stops at $x = x_{\max}$, and residue charges continuously flow from top electrode (Metal 1) to bottom electrode (Metal 2) to maintain electrostatic equilibrium; step III, the sliding part moves reversely from $x = x_{\max}$ to $x = 0$; step IV, the sliding part stops at $x = 0$, and the residue charges continuously flow from the bottom electrode to top electrode until the electrostatic equilibrium state, completing an entire cycle. (b) The voltage-charge (V - Q) plot of the CMEO with external load resistance of 150 M Ω , where the CMEO represents the maximum energy output in one cycle. The structural figure-of-merits under optimum resistance (FOM_{RS}) for (c) LS mode, (d) CFT mode, (e) SEC mode and (f) CS mode TENGs. The black lines represent the FOM_S for the corresponding modes of TENG, which are calculated under infinitely large resistances. The green arrow represents the figure-of-merits calculated at $x_{\max} = 0.45$ m. Reproduced with permission [49]. Copyright 2017, Elsevier.

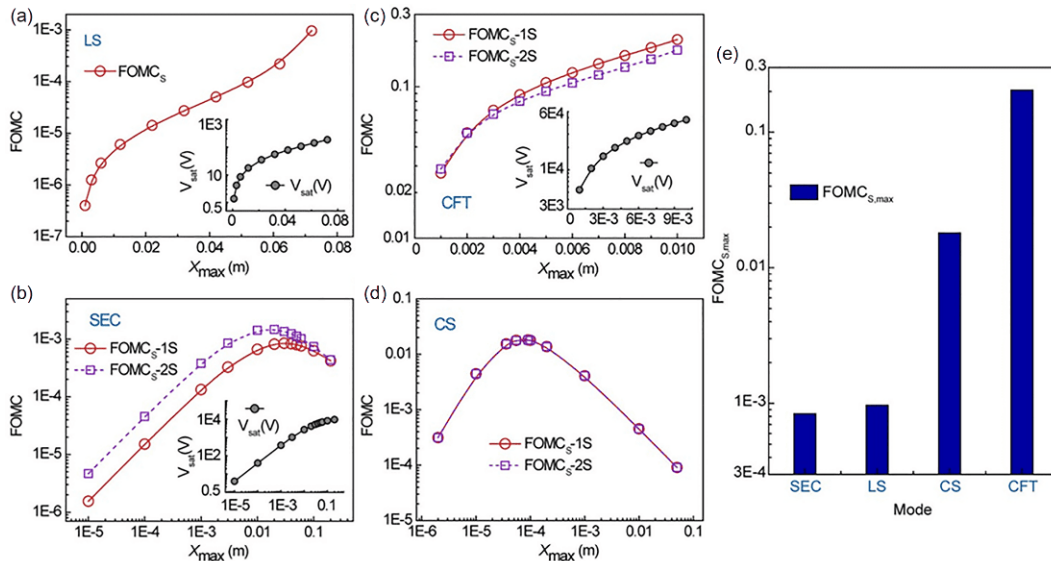


Figure 13 (Color online) FOM_S versus x_{\max} for four different TENG modes in a charging system. The FOM_S for (a) lateral sliding (LS) structure, (b) contact freestanding triboelectric-layer (CFT) structure, (c) single-electrode contact (SEC) structure and (d) CS mode TENGs calculated by analytical formulas. (e) Comparison of extracted maximum structural FOM (FOM_{S,max}) for the four basic modes of TENGs. The insets show the saturation voltage of the different load capacitances in the final charging cycles. 1S and 2S correspond to calculations considering 1-side and 2-side side effects of the TENGs. Reproduced with permission [32]. Copyright 2018, Elsevier.

inherent capacitance with the same x_{\max} when compared to other types of TENGs [44,49]. As a result, if a fixed transferred charge Q is given, the larger inherent capacitance leads to a lower E_m^C , resulting in a smaller FOMC_S. Furthermore, several conclusions should be noticed from these predictions. Firstly, the structural FOMC strongly relies on the structural parameters of TENGs and final charging cycle k , but is independent of the external capacitor C_L . Moreover, because the E_m^C can be practically obtained in a TENG charging system, the related FOMC_S are easily attainable and achievable, indicating its applicability to predict and assess the charging characteristics of TENGs.

5.4 Device and material figure-of-merits for power density

Peng et al. clarified the mechanism of power generation in TENG, optimized the output power from both the device capacitance and load resistance, and then defined a device figure-of-merit determining the maximum output power density of TENG at steady state [50]. Figure 14(a)–(c) shows the optimization principle of a contact-mode TENG through the matching between the mechanical motion frequency ω and the circuit characteristic frequency $1/RC_{\text{total}}$. When the TENG device has a larger $1/C_{\text{device}}$ due to the thicker dielectric layer, the $1/RC_{\text{total}}$ exhibits a smaller fluctuation close

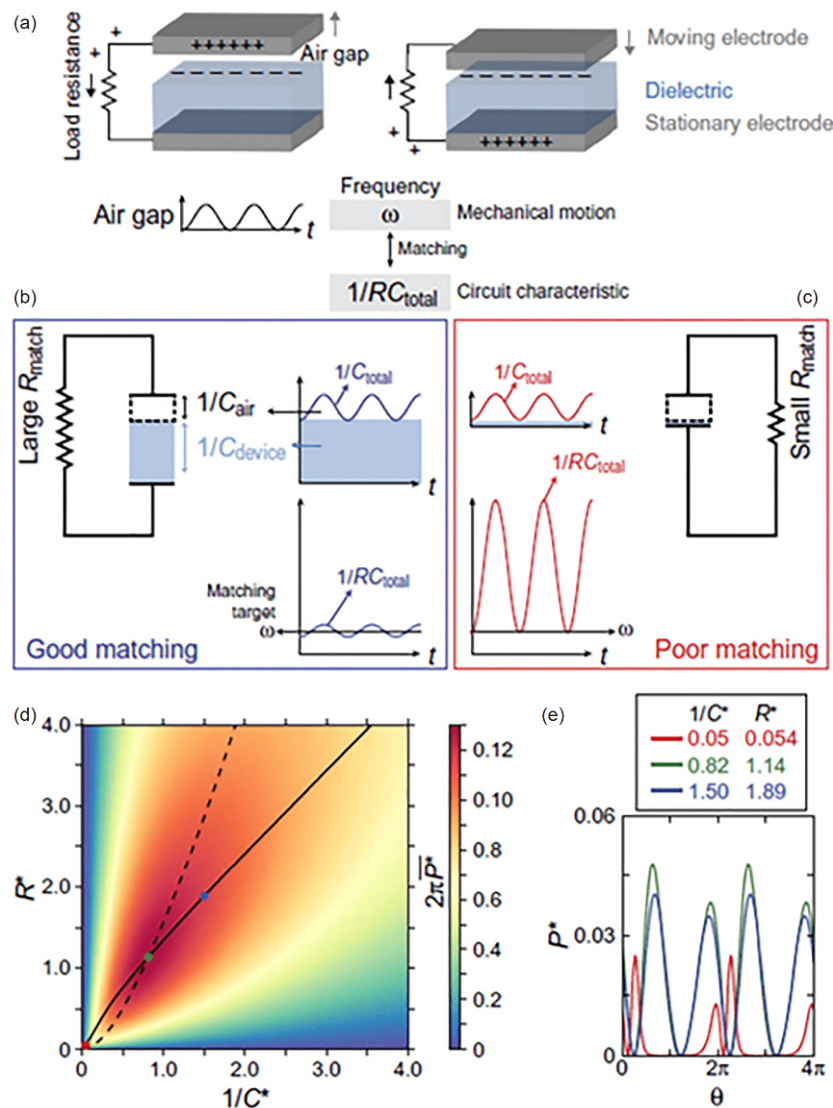


Figure 14 (Color online) (a) Schematic illustration of the working principle of a typical contact-mode TENG with a load resistor during the moving process of the top electrode. The air gap profile with respect to the time under external mechanical triggering with an angle frequency ω is shown, as well as the matching between the mechanical motion frequency ω and the circuit characteristic frequency $1/RC_{\text{total}}$; (b) a device circuit scheme with good matching when the circuit characteristic frequency $1/RC_{\text{total}}$ is close to the mechanical motion frequency ω . The device $1/C_{\text{device}}$ is large, and the load resistance is large; (c) another device circuit scheme with poor matching when the frequency $1/RC_{\text{total}}$ is far away from the frequency ω . The $1/C_{\text{device}}$ and load resistance are both small; (d) map of the dimensionless power per cycle $2\pi P^*$ of the TENG in steady state using an ideal model, presented in space of the two device parameters of R^* and $1/C^*$; (e) power P^* curves for the global optimum condition and two suboptimal conditions indicated in (d). Reproduced with permission [50]. Copyright 2017, AAAS.

to the ω , leading to a better matching. For any TENG with variable capacitance, decreasing the time variance of the RC product is critical for better matching to generate higher average power. However, to ensure the frequency matching, a larger $1/C_{\text{device}}$ induces a larger matched resistance R_L . Therefore, the power generation is optimized when both C_{device} and R_L are balanced. The advantage of the two-element optimization method (C_{device} and R_L) for enhancing the average power was demonstrated.

By converting the capacitance, resistance, power, etc. into dimensionless variables, an optimum condition was obtained for maximizing the dimensionless average power \bar{P}^* . The map of the dimensionless power per cycle $2\pi\bar{P}^*$ of the TENG at steady state in space of the two device parameters of R^* and $1/C^*$ was shown in Figure 14(d), indicating that the particular optimum condition is $R^*=1.14$, $1/C^*=0.82$, and $2\pi\bar{P}^*=0.127$. The power P^* curves for the global optimum condition and two suboptimal conditions were also presented in Figure 14(e). The optimum condition through optimizing both the R^* and $1/C^*$ produces the highest power. Based on that, a device figure-of-merit for power density was defined by

$$\text{FOM}_{\text{device}} = 0.064 \cdot \frac{\sigma^2 \bar{v}}{\varepsilon_0} \text{ (W/m}^2\text{)}, \quad (44)$$

where $\bar{v} = \omega x_{\text{max}} / \pi$ is the average motion speed, and the σ^2 is the material figure-of-merit FOM_M . It can be found that the $\text{FOM}_{\text{device}}$ is related with the FOM_M . The proposed $\text{FOM}_{\text{device}}$ expresses the actual maximum power density that could be obtained at a load resistor under optimized capacitance and

no parasitic reduction. Its definition and the corresponding optimization method could further promote the development of performance improvement of TENGs for practical applications.

6 Summary and perspective

This paper reviews the updated progress in constructing the general theoretical framework of triboelectric nanogenerators. Starting from the innovative extension of \mathbf{P}_s in the electric displacement vector \mathbf{D} , the Maxwell's equations have been expanded, based on which a systematic theory has been derived for quantifying the output and electromagnetic behavior of nanogenerators. The generation and variation of the Maxwell's displacement current, which is acted as the driving force of TENGs, has been calculated numerically through the built 3D mathematical model; in particular, for some special geometry cases, the analytical solutions have been obtained. Our basic conclusion is that the displacement current dominating the internal circuit is equal to the conduction current in the external circuit of TENGs. The basic output characteristics of the alternating current of TENGs have been investigated from the 3D mathematical model. Analytical formulae of obtaining the optimum resistance have been derived for getting the best output performances of TENG. In addition, the output performances of TENGs can be deeply understood by the CA model, which is proposed from the view of electric theory. Furthermore, figure-of-merits composed by a structural figure-of-merit related to the

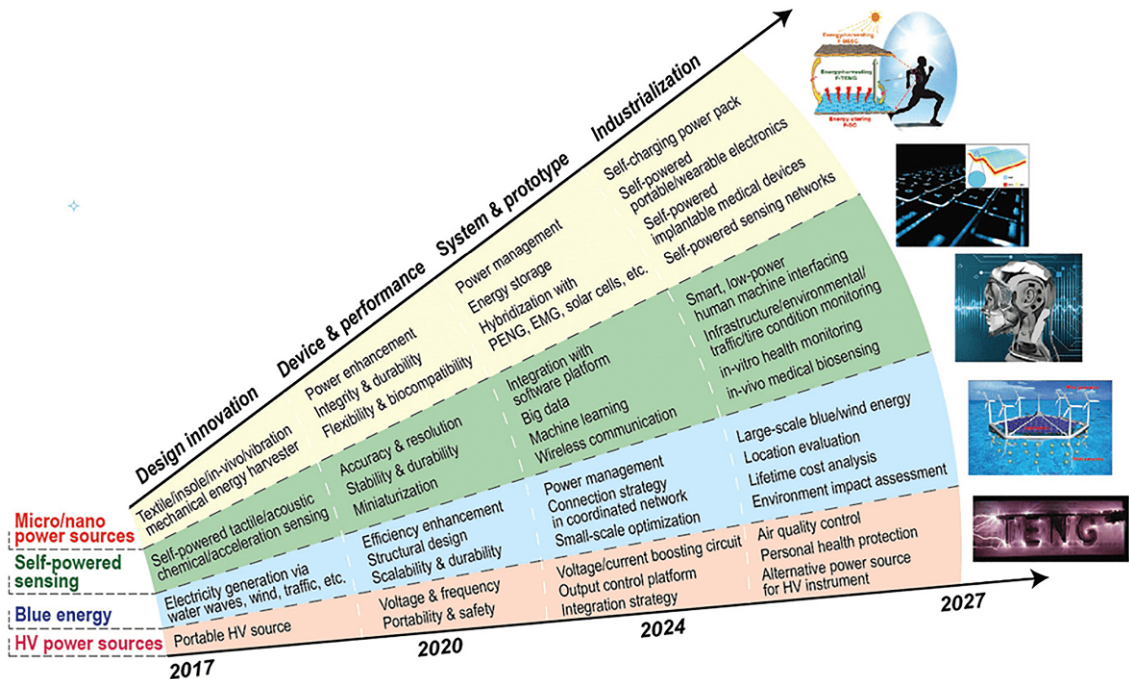


Figure 15 (Color online) Roadmap of the development of the TENG technology from 2017 to 2027 proposed based on the four important application fields of TENGs. Reproduced with permission [24]. Copyright 2018, Wiley-VCH.

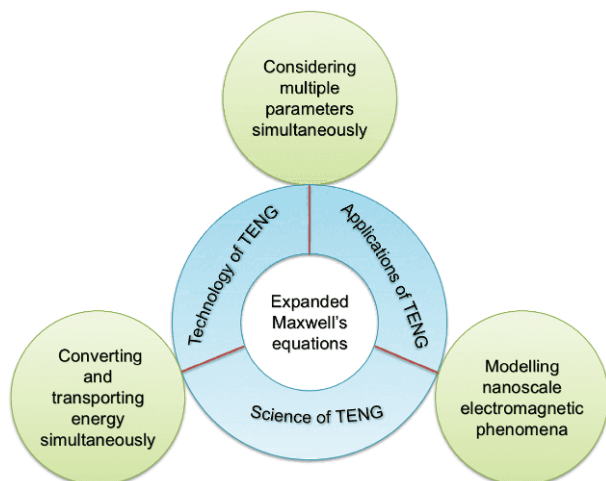


Figure 16 (Color online) Basic content and creative value in the three main aspects about the development of the theory of TENGs in the next step.

structure and a material figure-of-merit that is the square of the surface charge density, have been established and regarded as the standards for evaluating the performance of TENGs.

The established theoretical framework of TENGs sets the theoretical foundation of the future developments of the TENG technology in major application fields (Figure 15), from the structural design, performance optimization, to the system integration & prototype development, and finally to the industrialization. Although the general framework of TENGs has been built, we have to stress that the studies still have their own shortcomings, whether in the systematicness of the theory itself or applying the theory into practice. Therefore, here we anticipate that there should be three creative aspects in the next step (Figure 16). 1) reasonable structure, appropriate materials, and matched operation conditions of TENGs are always key parameters to determine the best outputs; enabling dimensional analysis and considering multiple parameters simultaneously may provide a more rational optimization strategy in the TENG system. 2) Based on the reformed Maxwell's equations, can we calculate the power delivered by a TENG if the operation frequency is extremely high? And can we make a special TENG that can convert and transport energy simultaneously? 3) Through the novel TENG device, we hope that the extended Maxwell's equations can be applied to other fields such as to model and understand nanoscale electromagnetic phenomena [51].

This work was supported by the National Key R&D Project from Minister of Science and Technology, China (Grant No. 2016YFA0202704), National Natural Science Foundation of China (Grant Nos. 51432005, 51702018, and 51561145021), Youth Innovation Promotion Association, CAS, and China Postdoctoral Science Foundation (Grant No. 2019M660766). We thank our group members and collaborators for their contributions to the

work reviewed here, especially Yunlong Zi, Simiao Niu, Morten Willatzen, Wei Tang, and Haiyang Zou.

- 1 Painuly J P. Painuly J P. Barriers to renewable energy penetration; a framework for analysis. *Renew Energy*, 2001, 24: 73–89
- 2 Khaligh A, Onar O C. Energy Harvesting: Solar, Wind, and Ocean Energy Conversion Systems. Boca Raton, FL: CRC Press, 2009
- 3 Wang Z L, Song J. Piezoelectric nanogenerators based on zinc oxide nanowire arrays. *Science*, 2006, 312: 242–246
- 4 Wang Z L. Nanogenerators, self-powered systems, blue energy, piezotronics and piezo-phototronics – A recall on the original thoughts for coining these fields. *Nano Energy*, 2018, 54: 477–483
- 5 Fan F R, Tian Z Q, Lin Wang Z. Flexible triboelectric generator. *Nano Energy*, 2012, 1: 328–334
- 6 Tang W, Jiang T, Fan F R, et al. Liquid-metal electrode for high-performance triboelectric nanogenerator at an instantaneous energy conversion efficiency of 70.6%. *Adv Funct Mater*, 2015, 25: 3718–3725
- 7 Zhu G, Zhou Y S, Bai P, et al. A shape-adaptive thin-film-based approach for 50% high-efficiency energy generation through micro-grating sliding electrification. *Adv Mater*, 2014, 26: 3788–3796
- 8 Xie Y, Wang S, Niu S, et al. Grating-structured freestanding triboelectric-layer nanogenerator for harvesting mechanical energy at 85% total conversion efficiency. *Adv Mater*, 2014, 26: 6599–6607
- 9 Lin L, Xie Y, Niu S, et al. Robust triboelectric nanogenerator based on rolling electrification and electrostatic induction at an instantaneous energy conversion efficiency of ~55%. *ACS Nano*, 2015, 9: 922–930
- 10 Zi Y, Guo H, Wen Z, et al. Harvesting low-frequency (<5 Hz) irregular mechanical energy: a possible killer application of triboelectric nanogenerator. *ACS Nano*, 2016, 10: 4797–4805
- 11 Wang S, Xie Y, Niu S, et al. Freestanding triboelectric-layer-based nanogenerators for harvesting energy from a moving object or human motion in contact and non-contact modes. *Adv Mater*, 2014, 26: 2818–2824
- 12 Wang S, Niu S, Yang J, et al. Quantitative measurements of vibration amplitude using a contact-mode freestanding triboelectric nanogenerator. *ACS Nano*, 2014, 8: 12004–12013
- 13 Bae J, Lee J, Kim S M, et al. Flutter-driven triboelectrification for harvesting wind energy. *Nat Commun*, 2014, 5: 4929
- 14 Quan Z, Han C B, Jiang T, et al. Robust thin films-based triboelectric nanogenerator arrays for harvesting bidirectional wind energy. *Adv Energy Mater*, 2016, 6: 1501799
- 15 Wang Z L. Catch wave power in floating nets. *Nature*, 2017, 542: 159–160
- 16 Wang Z L. Triboelectric nanogenerators as new energy technology and self-powered sensors – Principles, problems and perspectives. *Faraday Discuss*, 2014, 176: 447–458
- 17 Chen J, Yang J, Li Z, et al. Networks of triboelectric nanogenerators for harvesting water wave energy: A potential approach toward blue energy. *ACS Nano*, 2015, 9: 3324–3331
- 18 Jiang T, Zhang L M, Chen X, et al. Structural optimization of triboelectric nanogenerator for harvesting water wave energy. *ACS Nano*, 2015, 9: 12562–12572
- 19 Liang X, Jiang T, Liu G, et al. Spherical triboelectric nanogenerator integrated with power management module for harvesting multi-directional water wave energy. *Energy Environ Sci*, 2020, 13: 277–285
- 20 Xiao T X, Liang X, Jiang T, et al. Spherical triboelectric nanogenerators based on spring-assisted multilayered structure for efficient water wave energy harvesting. *Adv Funct Mater*, 2018, 28: 1802634
- 21 Xu L, Jiang T, Lin P, et al. Coupled triboelectric nanogenerator networks for efficient water wave energy harvesting. *ACS Nano*, 2018, 12: 1849–1858
- 22 Wang Z L, Chen J, Lin L. Progress in triboelectric nanogenerators as a new energy technology and self-powered sensors. *Energy Environ Sci*, 2015, 8: 2250–2282

- 23 Wang Z L, Jiang T, Xu L. Toward the blue energy dream by triboelectric nanogenerator networks. *Nano Energy*, 2017, 39: 9–23
- 24 Wu C, Wang A C, Ding W, et al. Triboelectric nanogenerator: A foundation of the energy for the new era. *Adv Energy Mater*, 2019, 9: 1802906
- 25 Niu S, Wang S, Lin L, et al. Theoretical study of contact-mode triboelectric nanogenerators as an effective power source. *Energy Environ Sci*, 2013, 6: 3576–3583
- 26 Niu S, Liu Y, Wang S, et al. Theory of sliding-mode triboelectric nanogenerators. *Adv Mater*, 2013, 25: 6184–6193
- 27 Niu S, Liu Y, Wang S, et al. Theoretical investigation and structural optimization of single-electrode triboelectric nanogenerators. *Adv Funct Mater*, 2014, 24: 3332–3340
- 28 Niu S, Liu Y, Chen X, et al. Theory of freestanding triboelectric-layer-based nanogenerators. *Nano Energy*, 2015, 12: 760–774
- 29 Wang Z L. On Maxwell's displacement current for energy and sensors: the origin of nanogenerators. *Mater Today*, 2017, 20: 74–82
- 30 Wang Z L. On the first principle theory of nanogenerators from Maxwell's equations. *Nano Energy*, 2020, 68: 104272
- 31 Shao J, Willatzen M, Shi Y, et al. 3D mathematical model of contact-separation and single-electrode mode triboelectric nanogenerators. *Nano Energy*, 2019, 60: 630–640
- 32 Shao J, Willatzen M, Jiang T, et al. Quantifying the power output and structural figure-of-merits of triboelectric nanogenerators in a charging system starting from the Maxwell's displacement current. *Nano Energy*, 2019, 59: 380–389
- 33 Shao J, Liu D, Willatzen M, et al. Three-dimensional modeling of alternating current triboelectric nanogenerator in the linear sliding mode. *Appl Phys Rev*, 2020, 7: 011405
- 34 Dharmasena R D I G, Jayawardena K D G I, Mills C A, et al. Triboelectric nanogenerators: Providing a fundamental framework. *Energy Environ Sci*, 2017, 10: 1801–1811
- 35 Maxwell J C. On physical lines of force. *Philosophical Magazine and Journal of Science*, Fourth series, London, Edinburgh and Dublin, 1861, 21: 161–175
- 36 Niu S, Wang S, Liu Y, et al. A theoretical study of grating structured triboelectric nanogenerators. *Energy Environ Sci*, 2014, 7: 2339–2349
- 37 Niu S, Zhou Y S, Wang S, et al. Simulation method for optimizing the performance of an integrated triboelectric nanogenerator energy harvesting system. *Nano Energy*, 2014, 8: 150–156
- 38 Niu S M, Liu Y, Zhou Y S, et al. Optimization of triboelectric nanogenerator charging systems for efficient energy harvesting and storage. *IEEE Trans Electron Devices*, 2015, 62: 641–647
- 39 Jiang T, Chen X, Han C B, et al. Theoretical study of rotary freestanding triboelectric nanogenerators. *Adv Funct Mater*, 2015, 25: 2928–2938
- 40 Jiang T, Chen X, Yang K, et al. Theoretical study on rotary-sliding disk triboelectric nanogenerators in contact and non-contact modes. *Nano Res*, 2016, 9: 1057–1070
- 41 Yao Y, Jiang T, Zhang L, et al. Charging system optimization of triboelectric nanogenerator for water wave energy harvesting and storage. *ACS Appl Mater Interfaces*, 2016, 8: 21398–21406
- 42 Shao J J, Tang W, Jiang T, et al. A multi-dielectric-layered triboelectric nanogenerator as energized by corona discharge. *Nanoscale*, 2017, 9: 9668–9675
- 43 Shao J, Jiang T, Tang W, et al. Studying about applied force and the output performance of sliding-mode triboelectric nanogenerators. *Nano Energy*, 2018, 48: 292–300
- 44 Niu S, Wang Z L. Theoretical systems of triboelectric nanogenerators. *Nano Energy*, 2015, 14: 161–192
- 45 Li X, Lau T H, Guan D, et al. A universal method for quantitative analysis of triboelectric nanogenerators. *J Mater Chem A*, 2019, 7: 19485–19494
- 46 Zi Y, Niu S, Wang J, et al. Standards and figure-of-merits for quantifying the performance of triboelectric nanogenerators. *Nat Commun*, 2015, 6: 8376
- 47 Jiang T, Tang W, Chen X, et al. Figures-of-merit for rolling-friction-based triboelectric nanogenerators. *Adv Mater Technol*, 2016, 1: 1600017
- 48 Zou H, Zhang Y, Guo L, et al. Quantifying the triboelectric series. *Nat Commun*, 2019, 10: 1427
- 49 Shao J, Jiang T, Tang W, et al. Structural figure-of-merits of triboelectric nanogenerators at powering loads. *Nano Energy*, 2018, 51: 688–697
- 50 Peng J, Kang S D, Snyder G J. Optimization principles and the figure of merit for triboelectric generators. *Sci Adv*, 2017, 3: eaap8576
- 51 Yang Y, Zhu D, Yan W, et al. A general theoretical and experimental framework for nanoscale electromagnetism. *Nature*, 2019, 576: 248–252